





RESEARCH ARTICLE | JANUARY 04 2023

Thermal effects on the performance of a nanosecond dielectric barrier discharge plasma actuator at low air pressure

Zongnan Chen (陳宗南) ; Chung Chu Wong (黃中柱) ; Chih-Yung Wen (溫志湧)  



Physics of Fluids 35, 017110 (2023)

<https://doi.org/10.1063/5.0127251>



CrossMark

Thermal effects on the performance of a nanosecond dielectric barrier discharge plasma actuator at low air pressure

Cite as: Phys. Fluids **35**, 017110 (2023); doi: 10.1063/5.0127251

Submitted: 20 September 2022 · Accepted: 9 December 2022 ·

Published Online: 4 January 2023



View Online



Export Citation



CrossMark

Zongnan Chen (陳宗南),¹ Chung Chu Wong (黃中柱),² and Chih-Yung Wen (溫志湧)^{2,a)}

AFFILIATIONS

¹Department of Mechanical Engineering, The Hong Kong Polytechnic University, Hong Kong, China

²Department of Aeronautical and Aviation Engineering, The Hong Kong Polytechnic University, Hong Kong, China

^{a)} Author to whom correspondence should be addressed: cywen@polyu.edu.hk

ABSTRACT

The thermal effects of a pulsed nanosecond dielectric barrier discharge plasma actuator (NSDBD) with varying pulse voltages and pulse repetitive frequencies under different air pressures ranging from 0.1 to 1 bar are studied experimentally. By observing discharge features with a charge-coupled device camera, the transition from a filamentary discharge mode to a diffuse mode with decreasing air pressure is described. The filamentary streamers extend along the radius direction, forming a thicker yet more stable and uniform plasma region due to the increasing ionized volume yielded by the decreasing air pressure to maintain the high values of the reduced electric field. The spatiotemporal temperature distribution on the surface is captured by an infrared camera, indicating that the heated surface can be divided into three typical regions with different features. Because gas heating is generated in the quenching process of excited molecules, the maximum temperature increase on the surface occurs in the plasma region and attenuates downstream. The surface temperature increase is primarily caused by heat convection from the residual heat in plasma and the heat generated by the dielectric losses. The results of heat flux on the surface suggest that the rising applied voltage may not increase the heat flux in a moderate air pressure ranging from 0.6 to 0.8 bar. Different discharge modes and discharge parameters exhibit markedly different thermal performances. Also, the Schlieren technique and the pressure sensor are used to visualize the induced shock wave, estimate the thermal expansion region, and measure the overpressure strength. The results of the overpressure strength at different air pressures are similar to the thermal features, which highlights the strong influence of the discharge mode on the thermal effect of NSDBD plasma actuators.

Published under an exclusive license by AIP Publishing. <https://doi.org/10.1063/5.0127251>

I. INTRODUCTION

Active flow control adds energy or momentum to airflow in a regulated manner and can be turned on or off as necessary, which has become a rapidly developing area over the past few decades.¹ Active flow control via plasma actuators has attracted a lot of attention in research due to its flexibility, high efficiency, and fast response. Active flow control has been widely applied to improve aerodynamic performance, including the elimination of flow separation on an airfoil,^{2,3} drag reduction,^{4,5} noise control,^{6,7} and suppression of the vortex-induced vibration of structures.^{8,9}

Typically, the working principle of plasma actuators is based on forming a low-temperature plasma through ionizing gas molecules between a pair of electrodes under a high voltage. Various plasma actuators are used based on different discharge types, such as corona, dielectric barrier, and spark discharges. A corona discharge is an

electrical discharge caused by the ionization of a fluid such as air surrounding a high-voltage conductor. An ionized wind will be generated near the wall when a pair of strip electrodes is set oppositely.¹⁰ A spark discharge is applied in different actuators, such as plasma synthetic jet actuators (PSJAs)¹¹ and localized arc filament plasma actuators (LAFPAAs).¹² A surface dielectric barrier discharge (DBD) plasma actuator, which is typically composed of four primary parts (a high-voltage power, an exposed electrode, an insulated electrode, and a dielectric barrier between these two electrodes) has been applied to a variety of flow control problems. For a DBD plasma actuator, the discharge features heavily depend on the input waveform. As a widely used flow control method, such as rolling moment control,^{13,14} a high-frequency alternative current voltage-driven DBD plasma actuator (ACDBD) is characterized by a relatively large-scale local flow motion known as ionic wind. Compared to ACDBD, nanosecond dielectric barrier

discharge plasma actuator (NSDBD) discharge supplied with a nanosecond-scale pulse duration has a much higher power density, leading to a fast-heating process. After each discharge pulse, energy deposition occurs quickly in the vicinity of the discharge streamers to form a strong thermalized area. This fast-heating process is essentially a direct excitation of molecules by electron impacts followed by fast quenching or decomposition with “hot” atom formation,¹⁵ which will be discussed in detail in Sec. III C. Then, an induced shock wave originates at each discharge streamer and propagates to the surrounding air.¹⁶ Therefore, the residual heat stemming from the energy deposition and the baroclinic vorticity caused by the interaction between the induced shock wave and the mainstream are the two fundamental characteristics of NSDBD plasma actuators, which have been regarded as control mechanisms. An ACDBD also releases thermal energy to the surrounding air.¹⁷ A series of ultrasounds was observed when an ACDBD was excited at a few kHz frequencies by Zhang *et al.*¹⁸ They hypothesized that the streamer discharge in the positive-going cycle plays an important role in generating the induced ultrasound.

NSDBD plasma actuators have been verified to be effective in active flow control, including the suppression of flow separation over an airfoil^{19–21} or a backward-facing step²² and control of the boundary-layer transition over a flat plate,²³ both experimentally and numerically. Recently, some studies have addressed supersonic flow control. An early attempt was made by Nishihara *et al.*,²⁴ who used an NSDBD plasma actuator to control a Mach-5 flow over a cylinder. Then, Bisek *et al.*²⁵ and Zheng *et al.*²⁶ numerically reproduced the flow phenomenon observed by Nishihara *et al.*²⁴ using a phenomenological model and a self-similar plasma model, respectively. They found that NSDBD plasma actuators effectively moved the standing bow shock with a minimum energy budget and that the drag of the cylinder decreased appreciably. Thus, a supersonic maneuver can be achieved by changing the normal force and pitching moment using NSDBD plasma actuators. Kinefuchi *et al.*^{27,28} experimentally and numerically investigated the control effects of NSDBD on flow separation induced by an impinging oblique shock over a flat plate. They found that the canted electrode can induce vorticity production, which results in momentum transfer from the primary flow to the boundary layer and consequently inhibits flow separation.

The aforementioned studies indicate that NSDBD is a novel and potential technology for subsonic and supersonic flow control. Thus, comprehensive investigations of the NSDBD’s characteristics in the

induced shock and energy deposition have attracted the attention of many researchers, which is of both fundamental and practical importance. Zhao *et al.*²⁹ investigated the induced shock waves and subsequent flow dynamics of an NSDBD plasma actuator and attributed the shock wave to a microblast. The time evolution of the shock pressure profile follows the Friedlander equation well. Zhang *et al.*³⁰ studied the induced shock wave and starting vortex features and found that the velocity of a starting vortex markedly increases with a short pulse rise time due to an increased reduced electric field E/N . For residual heat accumulation, Correale *et al.*¹⁶ measured the energy deposition region in different dielectric materials with various dielectric constants, volume resistivities, and thermal conductivities. They found that a high dielectric strength and a low volumetric resistivity are preferred for a barrier, together with a high heat capacitance and a low thermal conductivity coefficient, to maximize the efficiency of the thermal energy deposition induced by an NSDBD plasma actuator. Ndong *et al.*³¹ indicated that geometric parameters, such as the electrode length and gap, drastically modify the plasma behavior. According to the fast-heating process, the application of icing mitigation on aircraft was investigated.^{32–35} Liu *et al.*³⁶ investigated the unsteady heat transfer process over the airfoil/wing model exposed in frozen-cold airflows and found that the thermal characteristics are closely coupled with the boundary layer airflow. The anti-/deicing performance can be dramatically improved by increasing the pulse repetition frequency (PRF).

Table I shows the voltage, PRF, air pressure, and energy input involved in the current research on the NSDBD plasma actuator’s characteristics. Thereinto, for the thermal effects, Starikovskii *et al.*³⁷ estimated the gas temperature using emission spectra of 0 to 0 transition of the 2^+ system of the nitrogen molecule with an unresolved rotational structure. They found that the temperature increase is 40 K during the discharge phase and additional 100 K after 1 μ s in the first pulse on the discharge gap (energy input 11 mJ). Correale *et al.*³⁹ measured the surface temperature increase with different dielectric layer thicknesses and materials and quantified the heating efficiency of the NSDBD plasma actuator. In addition, for the low air pressure, Nudnova *et al.*⁴⁰ indicated fast gas heating is almost independent of pressure in the range 450–760 Torr (\sim 0.6–1 atm) under a low applied voltage between 17.5 and 20.5 kV. However, the temperature increase for 1 μ s reduces to 50–70 K at 300 Torr (\sim 0.4 atm). This change may be highly related to the discharge mode transition, which is a function of the applied high voltage and the gas pressure.⁴¹ However, to date,

TABLE I. Parameters given in the literature for the NSDBD plasma actuators’ characteristics.

Authors	Voltage (kV)	PRF (kHz)	Air pressure (atm)	Energy input (mJ/cm per pulse)
Starikovskii <i>et al.</i> , ^{19,37} 2009	12, 25, 50	One pulse	0.3–1.8	0.2–0.6
Takashima <i>et al.</i> , ³⁸ 2011	10–20	0.1–1	1	0.3
Little <i>et al.</i> , ³ 2012	15	0.01–1	1	0.3
Ndong <i>et al.</i> , ³¹ 2013	5, 10	0.01	1	0.2
Correale <i>et al.</i> , ^{16,39} 2015	10	0.1, 1	1	0.08
Nudnova <i>et al.</i> , ⁴⁰ 2015	17.5, 20.5	One pulse	0.4–1	0.5 mJ/mm ³
Liu <i>et al.</i> , ³⁶ 2019	10	1–6	1	0.2
Wei <i>et al.</i> , ³⁴ 2019	8	6	1	0.4
Zhang <i>et al.</i> , ³⁰ 2019	13.5	0.5, 1	1	0.5
Current study	25, 35	1, 2, 3	0.1–1	0.75–2

the thermal performance of an NSDBD plasma actuator is still unclear, which is considered a dominant mechanism, particularly under a wide range of air pressures from 0.1 to 1 atm in the troposphere where the air vehicles travel and with a high PRF. Therefore, the investigation of NSDBD thermal performance at low air pressure has practical importance in the field of active flow control. As a first step, this paper aims to systematically investigate the discharge characteristics of an NSDBD plasma actuator under different air pressures in the quiescent air with experiments and the corresponding efficiencies, as well as the effects of residual heat stemming from the energy deposition on the flow. Meanwhile, to compare with other research studies, extremely high applied voltages and frequencies are used to explore the application feasibility of NSDBD plasma actuators in the aeronautical industry.

The remainder of this paper is organized as follows. Section II describes the experimental setup. In Sec. III, the energy input measurement and discharge features captured by a charge-coupled device (CCD) camera at different air pressures are first discussed in detail. Then, temperature measurements using IR thermography on the surface are conducted in quiescent air to estimate heat deposition on and conduction to the dielectric surface. The surface temperature increase is characterized against various parameters, such as the applied voltage, frequency, and air pressure. The dynamics and strength of the induced shock and the evolution of the heated fluid are carefully discussed. Eventually, a comparison of the heating efficiency under various air pressures is made. Finally, conclusions are provided in Sec. IV.

II. EXPERIMENTAL SETUP

A. NSDBD plasma actuators

The NSDBD plasma actuator consists of two electrodes made of 0.01-mm-thick copper mounted on both sides of a dielectric layer, which was made of four layers of Kapton films with a total thickness of 0.02 mm. The spanwise length of the actuator was 100 mm, and the widths of the exposed (L_e) and insulated electrodes were 5 and 20 mm, respectively, as shown in Fig. 1(a). In this study, the long-insulated electrode is selected to maintain sufficient extension of the discharge streamers. There was no gap or overlap between the two electrodes. The actuator was placed flush on a 10-mm-thick acrylic flat plate as an insulated plane to prevent plasma formation below the dielectric layer. The insulated plane was placed on a thick foam plate to insulate the heat transfer from the bottom surface. The coordinate system was

constructed at the junction of the edges of the two electrodes, as shown in Fig. 1(a). The x axis coincides with the plasma streamer direction, and the y axis points in the vertical direction.

Voltages of 25 and 35 kV were applied by a nanosecond pulse generator (NPG 18/3500) with pulse repetition frequencies of 1000, 2000, and 3000 Hz. The applied voltage and current were measured using a high-voltage probe (Tektronix P6015A) and a current shunt probe (Megaimpulse CS-10/500), respectively. Both electrical signals were recorded by an oscilloscope (Agilent DSO-2014A) with a bandwidth of 100 MHz and a sampling rate of 2 GSa/s. In addition, a synchronization system was set up using a synchronizer (BNC Delay Pulse Generator 575-8C). A photocoupled circuit was used in the trigger system to reduce the electromagnetic interference (EMI) in the data acquisition system. The system was connected using high-voltage coaxial cables (RG 217) with four shielding layers.

The plasma actuator was mounted into a constant volume low-pressure chamber with three optical windows that were 200 mm in diameter [Fig. 1(b)]. The top optical window was made of silicon with a 95% transmittivity on the infrared wave and served as an observation window for the infrared camera. The discharge images and schlieren diagnostics were acquired through two side windows made of quartz. When performing a specific optical experiment, the irrelevant windows were covered with lids to avoid light getting inside the discharge chamber. The discharge chamber was pumped down to 0.1 to 1.0 bar in the experiments, and the initial pressure and temperature were monitored by a pressure transducer (Kulite XT-190SM-250A) and a thermocouple (TES-1310) mounted on the chamber bottom. According to the ideal gas equation of state, the temperature might decay slightly under a lower pressure when the volume is constant. The initial temperature in the discharge chamber decreases by 0.8 K from 1 to 0.1 atm. Table II shows the initial gas states of each case. In addition, the measurement uncertainty of the initial gas state is 1.7 kPa ($\sim 0.1\%$) and 0.1 K ($\sim 0.4\%$), for pressure and temperature, respectively, which lead to the density uncertainty of 0.02 kg m^{-3} ($\sim 1.6\%$) subsequently.

B. Infrared thermography and discharge visualization

The surface temperature of the NSDBD plasma actuator was measured using a midwave infrared camera (FLIR A6751 sc) with a 25-mm lens. Two calibrated temperature intervals ranging from 10 to

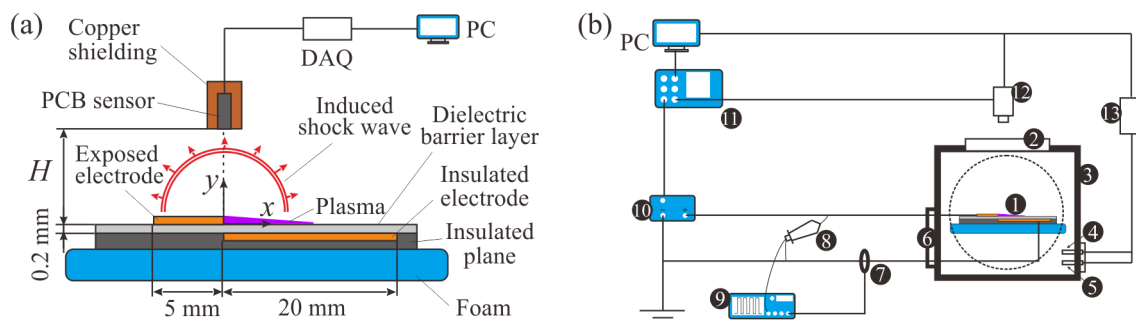


FIG. 1. (a) Schematics of the NSDBD plasma actuator and setup of the pressure sensor; (b) schematic representation of experimental setup. (1) Surface DBD plasma actuator, (2) observation window, (3) discharge chamber, (4) pressure transducer, (5) thermometer, (6) high-voltage flange, (7) current shunt, (8) voltage probe, (9) oscilloscope, (10) nanosecond pulse generator, (11) synchronizer, (12) infrared camera/CCD camera, and (13) data acquisition (DAQ) system.

TABLE II. Initial gas state in the discharge chamber.

Cases (bar)	1	0.8	0.6	0.4	0.2	0.1
P (Pa)	103 182.9	80 463.2	60 640.5	41 608.2	21 008.6	11 072.2
T (K)	295.61	295.42	295.58	295.65	294.98	294.84
ρ (kg m ⁻³)	1.215	0.948	0.715	0.490	0.248	0.131

90 and 35 to 150 °C were used, and the measurement accuracy was 0.018 °C. In this paper, the change in temperature ($\Delta T = T_t - T_{\text{initial}}$) is reported rather than the absolute temperature. After each test, the wall of the test section was removed to initialize the ambient condition. All diagnostics were performed at least three times, and comparisons of the results showed that the observations were repeatable. The initial temperature T_{initial} of the dielectric layer was measured before each experiment. The sampling frequency of the infrared camera was set at 100 Hz with a frame resolution of 4.2 pixels/mm. The infrared camera was installed above a silicon window mounted on the discharge chamber, which has a 95% transmissivity at infrared wavelengths. The surface heat flux can be calculated from the temperature time series using the one-dimensional semi-infinite model developed by Cook and Felderman.⁴² This method has been widely used to calculate the surface heat flux.^{39,43,44} The equation is

$$\dot{q}_n = 2\sqrt{\frac{\rho C_p k}{\pi}} \sum_{j=1}^n \frac{T_j - T_{j-1}}{\sqrt{t_n - t_j} + \sqrt{t_n - t_{j-1}}}, \quad (1)$$

where \dot{q}_n , T_j , and t_n are the heat flux, surface temperature, and time of step n , respectively; and ρ , C_p , and k are the density, specific heat capacity, and thermal conductivity of the model surface material. In this study, ρ , C_p , and k are equal to 1420 kg/m³, 1090 J/kg K, and 0.12 W/m K, respectively, for the Kapton tape used in the experiment. Notably, Kapton polyimide film retains its physical properties over a wide temperature range; especially, the density and specific heat capacity have almost no changes in the temperature range of the experiments. After a careful estimation,⁴⁵ the measurement uncertainty of thermal physical properties (caused by temperature) is neglected in this study.

In addition, a CCD camera (PCO.pixelfly) with a Nikon AF Micro lens (60 mm f1:2.8D) was used to visualize the plasma generated by the NSDBD plasma actuator. The camera exposure time was varied with the PRF to keep the same numbers of pulses covered during one exposure time. The sampling frequency was set at 10 Hz with a resolution of 1392 × 1040 pixels. The frame resolution was 14.35 pixels/mm.

C. Overpressure measurement

A fast-response dynamic pressure transducer (model PCB 132A31) was used to record the pressure profiles of induced shock waves. The pressure sensor was protected with copper shielding to weaken the electromagnetic interference and mounted facing normal to the actuator surface at the origin point, as shown in Fig. 1(a). The rise time of the sensor was less than 0.5 μ s, and the resolution is 7 Pa. The data were acquired by the DAQ device (Model NI Pxl-6368) at a sampling frequency of 2 MHz. A height gauge (model Mitutoyo 192-616) with a 0.05-mm resolution was used to measure the distance from the sensor center to the actuator surface.

D. Schlieren setup

A Schlieren technique was used to capture the shock structures and estimate their propagation velocities. This optical diagnostic technique is based on the variation in the medium refractive index caused by the change in the gas density.²⁹ The Schlieren system (WCL250G) was composed of a collimation and viewing system. A xenon lamp with an intensity of 80–300 mW/cm² was used as a light source. To obtain a high-resolution Schlieren image, a Nikon Nikkor Micro lens (105 mm f1:2.8D) was used, producing a spatial image resolution of approximately 0.11 mm/pixel. Shock structures were recorded using a high-speed camera (FASTCAM SA-Z type 2100K-M-32GB) with a resolution of 640 × 280 pixels. To record the propagation of the induced shock, the frame rate and shutter of the high-speed camera were set as 100 kHz and 0.25 μ s, respectively.

D. Uncertainty of the secondary parameters

To keep the confidence of secondary parameter's uncertainty as a function of measured parameter's uncertainty, the uncertainty propagation method was used in this study. Consider a derived quantity of interest y , which is a general function F of N measured variables x_i , with $i = 1, 2, \dots, N$.

$$y = F(x_1, x_2, \dots, x_N). \quad (2)$$

The variance of y is

$$\begin{aligned} \sigma_y^2 &= \sum_{i=1}^N \sum_{j=1}^N \frac{\partial F}{\partial x_i} \frac{\partial F}{\partial x_j} \rho(x_i, x_j) \sigma_{x_i} \sigma_{x_j} \\ &= \sum_{i=1}^N \left(\frac{\partial F}{\partial x_i} \right)^2 \sigma_{x_i}^2 + 2 \sum_{i=1}^{N-1} \sum_{j=i+1}^N \frac{\partial F}{\partial x_i} \frac{\partial F}{\partial x_j} \rho(x_i, x_j) \sigma_{x_i} \sigma_{x_j}, \end{aligned} \quad (3)$$

where $\rho(x_i, x_j)$ is the cross-correlation coefficient between x_i , x_j , defined by

$$\rho(x_i, x_j) = \text{cov}(x_i, x_j) / \sigma_{x_i} \sigma_{x_j}. \quad (4)$$

When x_i and x_j are statistic independent, $\rho(x_i, x_j) = 0$ [$\text{cov}(x_i, x_j) = 0$] and the Eq. (3) reduces to

$$\sigma_y = \sqrt{\sum_{i=1}^N \left(\frac{\partial F}{\partial x_i} \right)^2 \sigma_{x_i}^2}. \quad (5)$$

Similarly, the uncertainty of a derived parameter y is

$$\Delta y = t \sigma_y = \sqrt{\sum_{i=1}^N \left(\frac{\partial F}{\partial x_i} \right)^2 \Delta_{x_i}^2}. \quad (6)$$

Here, t is the confidence coefficient.

III. RESULTS AND DISCUSSION

To comprehensively investigate the thermal effects of NSDBD, the energy input and discharge features are studied in detail first. Then, surface temperature measurements using IR thermography are conducted in quiescent air to estimate the heat deposition on and conduction to the dielectric surface. The surface temperature increase is characterized by various parameters, such as the applied voltage,

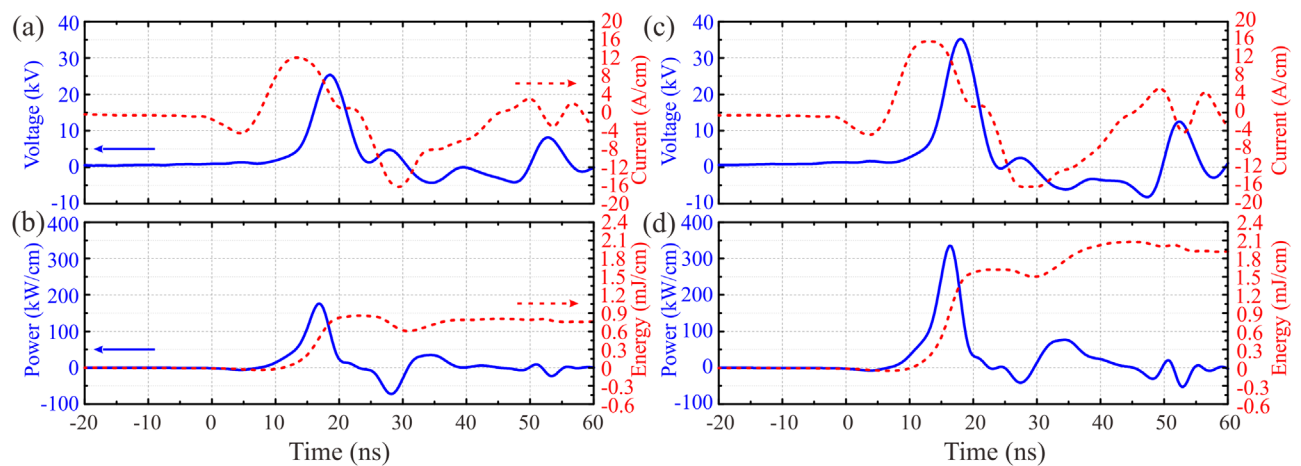


FIG. 2. Electrical aspects of a positive pulse discharge: voltage and current at (a) 25 and (c) 35 kV, power and energy at (b) 25 and (d) 35 kV at $P=0.1$ bar.

frequency, and air pressure, and the underlying physical mechanisms are carefully analyzed. The dynamics and strength of the induced shock and the evolution of the heated fluid are presented. At last, the efficiency of surface heating is discussed.

A. Energy input at different air pressures

First, the electrical properties of discharge in this study are investigated. Figures 2(a) and 2(c) show typical waveforms of the applied voltage and the current of unit length for a positive polarity discharge at 0.1 bar. The measured peak voltage amplitudes are 25 kV [Fig. 2(a)] and 35 kV [Fig. 2(b)], respectively, with a duration time of approximately 10 ns. The results shown are average values of five repeated measurements. Also, the measurement uncertainties are listed in Table III, and the confidence coefficient is 3. Both cases share a short rise time of 4 ns. A shorter rise time leads to an increase in the current amplitude and a rapid energy deposition from the pulsed generator to the plasma actuator.

The maximum currents are approximately 12 and 16 A/cm for the peak voltage cases of 25 and 35 kV, respectively, during the voltage rise time. This current peak is caused by charge deposition resulting from discharge near the exposed electrode when the electric field is sufficient to initiate air breakdown. Following the first peak, there is no obvious silent period due to an extremely short duration time. The subsequent negative current trough occurs during the fall time of the voltage, where a new discharge occurs with a sufficient potential difference. These current peaks and troughs manifest an asymmetry associated with the completely different discharge regimes.³¹ Typical waveforms of the electric power and energy are shown in Figs. 2(b) and 2(d).

TABLE III. Uncertainties of parameters under 0.1 bar at 25 and 35 kV in Fig. 2.

Case (0.1 bar)	Voltage (V)	Current (A/cm)	Power (kW/cm)	Energy (mJ/cm)
25 kV	200 (0.8%)	0.41 (3.4%)	10.5 (3.5%)	0.0164 (3.5%)
35 kV	315 (0.9%)	0.47 (2.9%)	17.2 (3.1%)	0.0269 (3.1%)

The power peak results from the power transfer through the supply to the actuator. The energy input of each pulse, integrated by the instantaneous power, reaches an asymptotic quantity of approximately 0.75 mJ/cm at 25 kV and 1.95 mJ/cm at 35 kV at the end of the voltage pulse.

Figure 3 plots the energy inputs as a function of the gas pressure for the cases of 25 and 35 kV. The energy inputs are approximately 7.5 mJ/pulse at 25 kV and 20 mJ/pulse at 35 kV with the 100 mm spanwise length of the actuator. The energy input increases with the applied voltage and depends on the gas pressure only marginally, which is coincident with Nudnova’s observation.⁴⁰ The PRF used in measurements of the electrical properties of discharge is fixed at 1 kHz. According to Zhang’s work,³⁰ the PRF does not affect the electrical parameters.

B. Discharge characteristics

In this section, the effects of the air pressure, voltage amplitude, and PRFs on discharge streamers are examined. The transformation

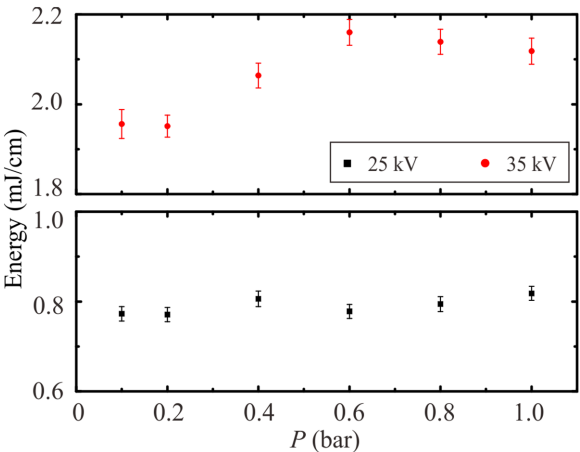


FIG. 3. Energy input per unit length vs pressure at 25 and 35 kV.

between two discharge modes—diffuse mode and filamentary mode—is captured using CCD images.

1. Effects of air pressure

Figure 4 shows images of a repetitive nanosecond pulse discharge taken with a CCD camera under different air pressures and PRFs. The camera exposure time was adjusted to keep ten discharge pulses during the exposure to each PRF case. All images are acquired after 10 000 pulses. The locations of the exposed and insulated electrodes are marked by the gray strip and dashed line, respectively, in the upper-left image (35 kV, PRF of 1 kHz and 1 bar). Considering the higher voltage case of 35 kV at 1 kHz as an example at atmospheric pressure [the first column in Fig. 4(a)], the discharge is composed of many streamers distributed along the length of the exposed electrode. The discharge streamers propagate in a filamentary structure in the direction of the insulated electrode and form a plume-like shape at the streamer end. These branching structures occur in the decaying period of the positive voltage pulse, and there is a lower density of charges and a reduced number of streamer channels compared to the process in the rising period. The location, shape, and intensity of individual filaments are fairly random due to a series of orderless discharge channels.⁴⁶ When the discharge is sufficiently strong, these distinct channels are distributed discretely. Although some filaments tend to form at nearly the same positions, they are not caused by defects on the electrodes. These inhomogeneous and separated channels characteristic of the discharge are summarized as the filamentary mode.⁴⁷ This mode is believed to be a contractive state of the discharge channel caused by the instability of radial perturbations.⁴⁸ Gas heating is an

important reason for this instability. For the lower voltage case of 25 kV at 3 kHz [the first column in Fig. 4(d)], the surface discharge is less intense but also keeps the filamentary features.

When the air pressure decreases to 0.8 bar [the second column in Fig. 4(a)], the discharge channel width decreases and becomes denser. This change makes the filaments distribute more uniformly, prompting the transformation to diffuse mode. With the decrease in air pressure to 0.6 bar, the filaments disappear, and the plasma luminosity descends significantly, as shown in Fig. 4(b). The plasma distributes quasi-homogeneity along the electrode edge, presenting as the filamentary/diffuse mixed mode. Several discharge streamers with a higher luminosity can still be observed in this mode, which indicates that the surface discharge supplied by a repetitive nanosecond pulse was a microfilament discharge, which primarily consisted of a series of discharge channels. At 25 kV, the transformation will be delayed to a lower air pressure condition of 0.4 bar, even at a high PRF of 3 kHz. In addition, the discharge remains nearly constant when the air pressure drops from 1 to 0.8 bar, which can be attributed to the relatively low applied voltage inducing a marginally weaker discharge, which is less susceptible to air density, particularly in the relatively high range of air pressure.

As the air pressure drops further from 0.4 to 0.2 bar [the fifth column in Fig. 4(a)], the discharge gradually becomes a diffuse mode presented as a glow-like discharge. This result should be distinguished from the glow discharge, which has a distinct discharge formation mechanism. As shown in Figs. 6(c) and 6(d), both plasma length and thickness increase with the descending air pressure because the ionized volume should be increased due to the sparse air to maintain the high values of the reduced electric field (E/N). The expansion of discharge

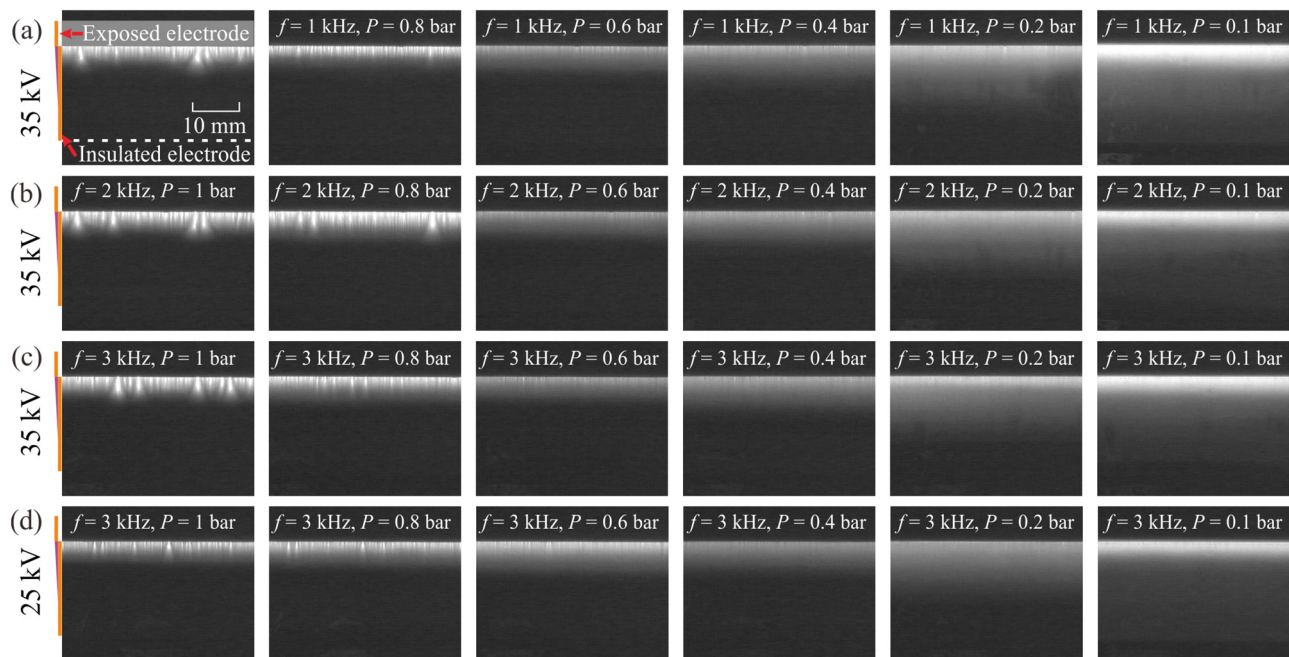


FIG. 4. Images of the discharge at different gas pressures at PRF of (a) 1, (b) 2, (c) 3 at 35 kV, and (d) 3 kHz at 25 kV. The exposure time is set as ten pulses after the 10 000th pulse.

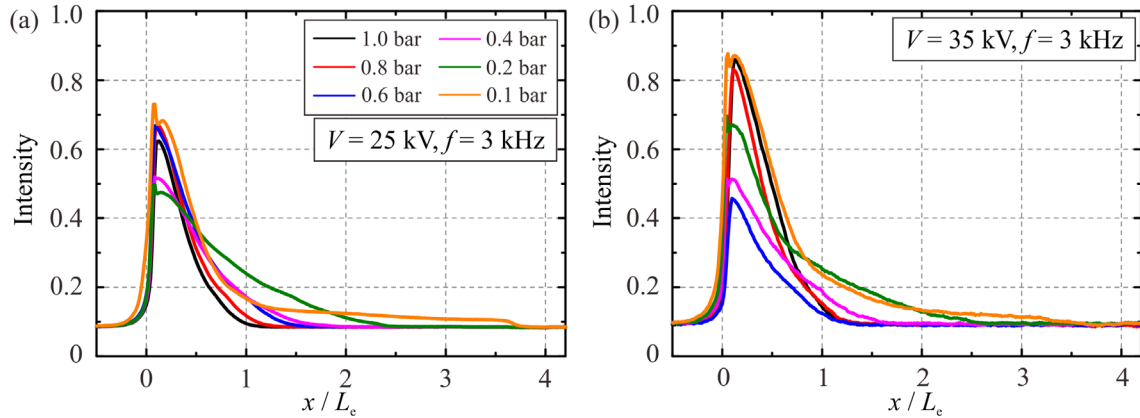


FIG. 5. Normalized luminous intensity vs dimensionless length along the x direction at (a) 25 kV and (b) 35 kV of 3 kHz PRF.

channels leads to a more stable state toward the radial direction, which accounts for the absence of microfilaments. This trend is manifested at the lowest air pressure of 0.1 bar.

As the air pressure drops from 1 to 0.1 bar, the discharge undergoes the transition from the filamentary mode to the mixed mode and the diffuse mode. The filamentary streamers extend along the radius direction, forming a larger yet more stable and uniform plasma region. The current for a diffuse discharge mode also occurs earlier than that for a filamentary discharge, indicating that rapid heat is faster in the former discharge mode. The plasma luminosity reduces to the minimum in the mixed mode and increases again in the diffuse mode for both cases of 25 and 35 kV (averaged results in Fig. 5). Due to the plasma volume increase in the diffuse mode, the plasma region tends to have a larger luminosity. Figure 6 shows the plasma length and thickness, which are estimated from the position with a 5% maximum normalized luminous intensity captured by CCD images, and the exposure time is set as one pulse in this study. The results are averaged over repeated measurements, and the standard errors are marked. In filamentary mode, the plasma length and thickness barely change, particularly for the 35 kV case. When the discharge transforms to the

diffuse mode, they increase exponentially with decreasing air density. In general, an increase in the voltage amplitude results in a growth of plasma volume. The voltage increase will increase the longitudinal and transverse components of the local electric fields. The increase in the transverse electric field causes a thicker plasma layer. In contrast, the longitudinal electric field increase leads to a larger ionization wave speed, leading to a plasma layer length growth.⁴⁰ However, the two voltage cases examined in this study share little difference in the plasma volume. When the applied voltage reaches 25 kV, the discharge becomes saturated in the plasma volume. The persistent increase in voltage causes a radius growth of filamentary channels, forming a plume-like structure instead of the plasma volume growth. The filament-to-diffuse transition is a common feature as a function of the amplitude and polarity of the applied voltage, the gas pressure, and the gas mixture composition.⁴¹

2. Effects of PRF

Each column of Figs. 4(a)–4(c) shows discharge images of 35 kV at different PRFs with the same air pressure. Results indicate that

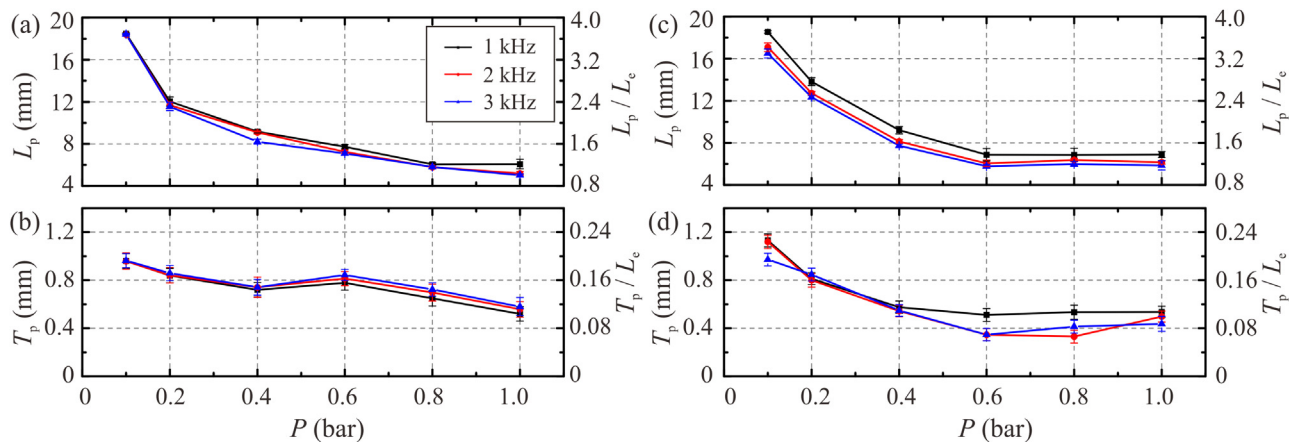


FIG. 6. Plasma length and thickness at (a) and (b) 25 kV and (c) and (d) 35 kV vs air pressure.

the PRF does weakly affect the streamer distribution, luminosity, and discharge mode transition within the current air pressure range. These results imply that although the plasma accumulation grows in a fixed time interval, the discharge formation mechanism is nearly unchanged. The discharge intensity weakens at an air pressure of 0.1 bar and a PRF of 2 and 3 kHz [the sixth column in Figs. 4(b) and 4(c)]. At high voltage and low air density, the air in the vicinity of the exposed electrode cannot maintain an intense discharge. The discharge intensity will attenuate to accommodate the increased PRF, which can strongly influence the residual heat deposition. Similar observations can be made for the plasma length and thickness [Figs. 6(c) and 6(d)], which tend to diminish with increasing PRF. In addition, the PRF rarely affects the discharge properties in a lower voltage amplitude case of 25 kV. However, the PRF plays an important role in flow control because the interrelation between the residual heat accumulation and the characteristic time in flow can strongly improve the control efficiency, as discussed in Sec. III C.

C. Heat transfer on the dielectric layer surface

The gas heating process of an NSDBD plasma actuator is primarily caused by the complex collisions, reactions, and interactions between energetic electrons, ions, and excited molecules generated in the plasma region.³⁰ Driven by the intense electrical field, energetic electrons impact N_2 and O_2 molecules, which will be excited to high electronic states from the ground state. Then, these excited molecules can be dissociated by electron impact. The dissociation leads to the transfer of the excess energy into the translational degrees of freedom of the produced oxygen atoms. The energy released in collisions of thermalized oxygen atoms is expended on the rotational excitation of molecules and gas heating, and the rotational energy relaxes into the translational energy during multiple collisions.⁴⁹ The kinetic energy in this quenching process is rapidly transferred into the surrounding gas.

In addition to the collisional quenching of excited electronic states of N_2 molecules by O_2 , the excited oxygen atoms $O(^1D)$ quenched primarily by O_2 and N_2 molecules also provide excitation energy to the gas heating. The quenching process of the excited oxygen atoms $O(^1D)$, which are generated in O_2 dissociation, proceeds through the formation of an intermediate complex.⁵⁰ These two

quenching processes dominate the heat transfer on gas heating at $E/N \leq 200$ Td, while at $E/N > 400$ Td, the dissociation reactions of N_2 molecules by electron impact and the processes involving charged particles make the primary contribution.⁵¹ Another important contribution to gas heating when the degree of dissociation of O_2 molecules is sufficiently high is the reaction of the vibrational-translational relaxation of the vibrational levels $N_2(\nu)$ by excited oxygen atoms $O(^3P)$. This process is considered to provide slow heating that occurs on a time scale of approximately 200 μs .⁵² In this section, the heat transfer caused by residual heat on the surface was studied. The surface temperatures were spanwise averaged by repeated measurements. The uncertainty is 0.27 K ($\sim 0.6\%$ of peak value) in the rapid temperature increase stage (10 s), for the case under 0.8 atm and actuated at 3 kHz PRF and 25 kV. Here, the heat flux uncertainty and residual heat uncertainty were roughly estimated by root mean square errors of arithmetic mean values of repeated measurements with the confidence coefficient of 3, which are 101.5 W/m² ($\sim 2.2\%$ of peak value) and 0.0054 W ($\sim 1.4\%$ of peak value), respectively.

1. Surface heating behaviors in long-term activation

A longer-duration case of 250 s in standard air pressure was investigated first to gain the global characteristics of surface heat transfer. In this study, ten Kapton film layers each with a thickness of 0.5 mm and an applied voltage of 22 kV were used to avoid surface material failure caused by residual heat. All data were averaged along the spanwise direction. Figure 7(a) plots the time variation of temperature rise at $x/L_e = 0.2$ with different PRFs. The entire temperature increase can be divided into two stages: a rapid temperature increase in the initial 10 s and then slow growth until a steady-state value at long times. A high PRF strongly increases the heat accumulation in the same period. The surface temperature increases with the operation time, analogous to the exponential curves. Figure 7(b) shows the heat flux variations at $x/L_e = 0.2$ calculated by the one-dimensional semi-infinite model. In the rapid increase stage, the heat flux rises quickly and reaches a peak value, which indicates that the heat in the discharge transfers to the surface of the dielectric layer in a short time. Then, the heat flux decreases to a steady value, which implies that the temperature increase slows down gradually, and heat transfer achieves

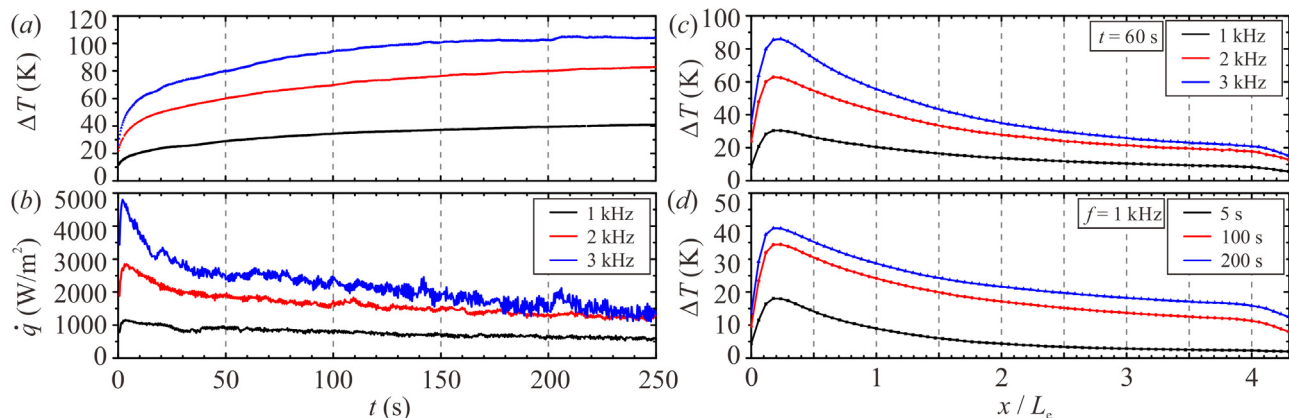


FIG. 7. (a) Temperature increase with time at $x/L_e = 0.2$; (b) heat flux variation with time at $x/L_e = 0.2$; (c) temperature increase along the x direction at $t = 60$ s with different PRFs; (d) temperature increase along the x direction at PRF $f = 1$ kHz at different times.

a balance when the heat increment from the gas equals the heat dissipation in the dielectric substrate. This process can also be observed in spanwise-averaged temperature changes at different times, as shown in Fig. 7(d). The streamwise (x direction) variation in the temperature increase at $t = 60$ s with different PRFs is shown in Fig. 7(c). The distribution is similar to that in early work of Correale *et al.*³⁹ The highest temperature occurs near the edge of the electrode ($x/L_e = 0.2$) and gradually reduces downstream in the insulated electrode direction, attaining a value near room temperature. No noteworthy changes are observed between the PRF cases in terms of the tendency to increase the temperature distribution.

The corresponding spatiotemporal variations in the spanwise-averaged temperature at PRFs of 1, 2, and 3 kHz are plotted in Fig. 8 as contour fields. The horizontal axis is the dimensional length in x distance, and the vertical axis is the time. The dashed lines mark the edge of the insulated electrode. According to the spatiotemporal temperature distribution, the dielectric surface can be divided into three typical regions in the streamwise direction distinguished by two inflection points (red dots in Fig. 8): the plasma region, the insulated electrode region, and the far-field region.¹⁷ Large temperature increases are observed near the exposed electrode corresponding to the plasma region ($0 \leq x/L_e \leq 1$). At 1 kHz, the temperature increment reached 40 K at $t = 220$ s but only takes several seconds to approach 40 K in the 3 kHz case. The denser isotherms near the exposed electrode during the early period after activation also indicate this rapid increase stage, particularly in the high PRF case. Because the plasma is the dominant heating source, the spanwise-averaged surface temperature is much higher than that in the other two regions. Due to the absence of plasma, the surface temperature in the insulated electrode region is low. Although the temperature continues to grow in this region, the growth rate has become moderate. The first inflection point in the isotherms also highlights this change. The temperature increase in the dielectric surface is caused by the heat generated by the dielectric losses and the heat transfer from the residual heat in plasma. This process exchanges the thermal energy from the induced flow, although it is small for an NSDBD plasma actuator. Part of the thermal energy in

the dielectric layer is transferred to the far-field region through internal thermal conduction. In the far-field region, the surface temperature drops considerably near the edge of the insulated electrode, which is indicated by the second inflection point in the isotherms. The local heating in this region is provided by thermal convection with the ambient air and internal thermal conduction from the upstream areas. The thermal conduction inside the dielectric layer is slow due to the small thermal conductivity of the dielectric material of only 0.12 W/m K, compared to that of the copper electrodes, which was approximately 400 W/m K.

2. Surface heating behaviors at different air pressures

In this section, the rapid temperature increase stage around the first 10 s is chosen to investigate the thermal characteristics of varying air pressures. Examples of instantaneous surface temperature increases at 35 kV are plotted in a top view of the plasma actuator in Fig. 9. Three different air pressure conditions of 0.2, 0.6, and 1 bar are selected to represent three typical discharge modes for comparison. The isotherms of 2, 5, 10, 20, and 40 K are marked with solid black lines. As shown in Figs. 9(c1)–9(c3) (Multimedia view), in a standard atmosphere, the discharge leads to an inhomogeneous temperature increment in the spanwise direction near the exposed electrode ($0 \leq x/L_e \leq 1$). In all three PRF cases, the high-temperature spots concentrate from $x/L_e = 0$ to 0.5 (Fig. 8), where the maximum temperature rise is more than twice that in the streamer head of $x/L_e = 1.4$. Babaeva *et al.*⁵³ indicated that the predicted ionization occurs primarily in the streamer head and propagates downstream under a high electric field in a positive nanosecond pulse discharge. The electrical field reduces quickly on the dielectric surface, leading to an attenuated ionization source and the deceleration of the ionization wave. Because gas heating is generated in the quenching process of excited molecules, the local strength of the electron impact ionization source strongly affects the temperature rise in the gas. The weakened gas heating along with the streamer channel direction is a result of the ionization attenuation starting from the streamer head propagating downstream. Most gas heating concentrates on the upstream side of discharge streamers. In the mixed mode at 0.6 bar, as shown in Figs. 9(b1)–9(b3), the increase in temperature becomes uniform along the spanwise direction. The high-temperature spots corresponding to the filamentary streamers disappear gradually. Considering PRF of 2 kHz as an example, the isotherm of 2 K is located on average at $x/L_e = 2.1$ [Fig. 9(b2)], which is the smallest among the cases of $x/L_e = 2.6$ [Fig. 9(a2)] at 0.2 bar and $x/L_e = 3.1$ [Fig. 9(c2)] at 1 bar. This result indicates that the heating region decreases streamwise when the filaments shrink with decreasing air pressure and increase again due to the plasma volume growth at a lower air density at 0.2 bar. Although PRFs rarely affect discharge features, the heating region and the maximum temperature rise increase markedly with increasing PRF in all pressure cases of the same energy input after 10 000 pulses. While a more homogeneous surface temperature along the streamwise direction is observed at 0.2 bar [Figs. 9(a1)–9(a3)], the temperature rise in the upstream side of the plasma is also much more evident, which is consistent with the observation of the most intense discharge [see the sixth column in Fig. 4(b)].

Based on the measured surface temperature increase distribution, the spanwise-averaged spatiotemporal profiles at the different air pressures and PRFs in the rapid increase stage are plotted in Fig. 10.

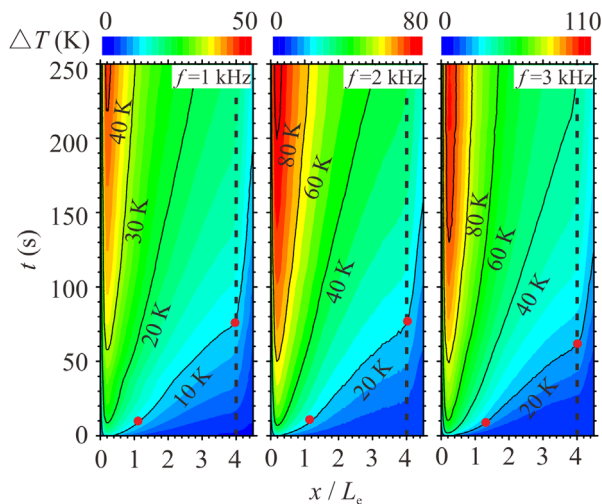


FIG. 8. Spanwise-averaged spatiotemporal temperature distribution of the NSDBD plasma actuator at different PRFs.

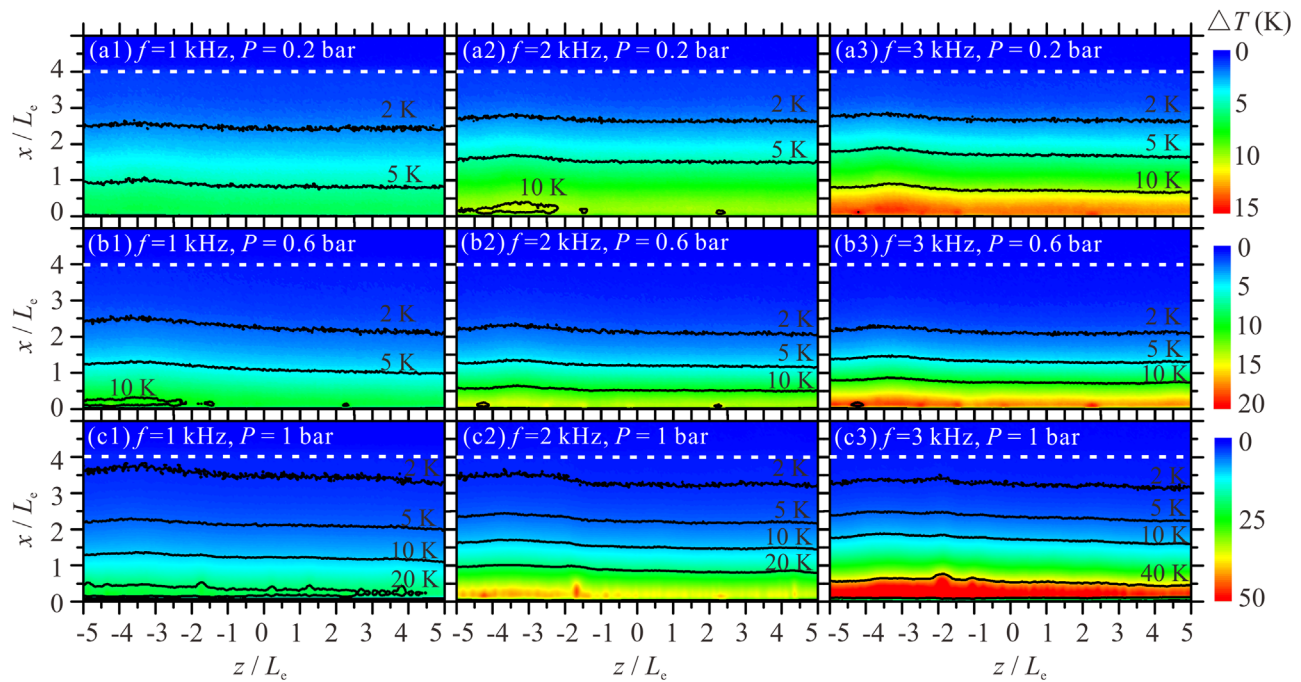


FIG. 9. Instantaneous surface temperature distributions after the 10 000th pulse at 35 kV in the cases of (a1) 1, (a2) 2, (a3) 3 kHz at 0.2 bar; (b1) 1, (b2) 2, (b3) 3 kHz at 0.6 bar; and (c1) 1, (c2) 2, (c3) 3 kHz at 1 bar. Multimedia view: <https://doi.org/10.1063/5.0127251.1>

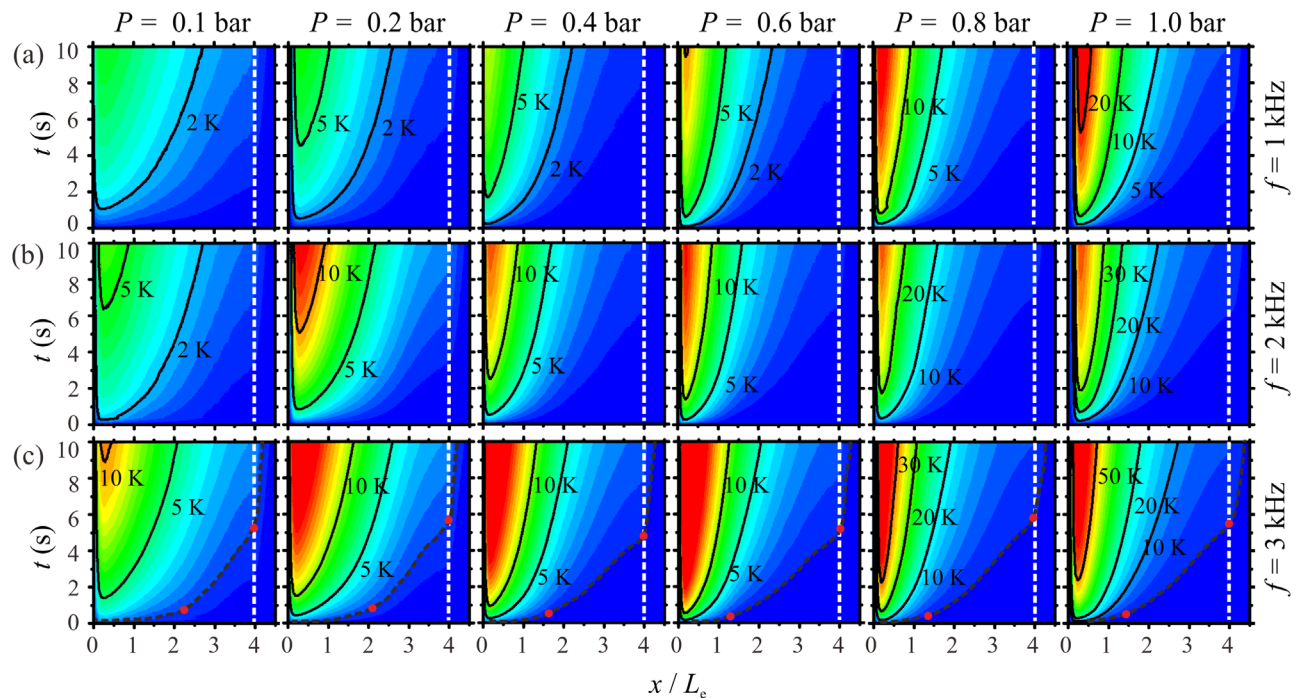


FIG. 10. Spanwise-averaged spatiotemporal temperature distributions of the NSDBD plasma actuator at PRF = (a) 1, (b) 2, and (c) 3 kHz with different air pressures at 35 kV. The dashed line indicates the edge of the insulated electrode.

Isotherms at 2, 5, 10, 20, and 30 K are extracted with solid lines. The three typical regions can still be distinguished by the isotherm at a low temperature (marked by the black dashed line), which pervades all spatiotemporal ranges. In the far-field region divided by the edge of the insulated electrode, the temperature is nearly unchanged in the rapid temperature increase stage in all cases. This result is likely caused by slow thermal conduction inside the dielectric layer and the long distance from the upstream heated gas. The steep slope of this isotherm in the far-field region also suggests a tenuous temperature change, particularly in low air pressure cases. In contrast, the subdued slope implies that the temperature rises nearly synchronously in this region, which can present the plasma region's heating features well. In addition, the intensive isotherms indicate a more significant temperature growth rate. In the plasma region, the temperature growth rate decreases with more tenuous air, independent of the discharge mode. The maximum temperature markedly decreases from the filamentary mode to the diffuse mode but only marginally decreases from 0.4 to 0.2 bar in the diffuse mode.

To evaluate the heating process on the surface in more detail, the heat flux is calculated using the one-dimensional semi-infinite model, as shown in Fig. 11. The residual heat power on the dielectric layer above the insulated electrode region (from $x/L_e = 0$ to 4) is integrated and plotted in Fig. 12. The heat flux distribution indicates that the maximum occurs around $x/L_e = 0.2$ ($x = 1$ mm), independent of the applied voltage and PRF, which is consistent with the observation by Correale *et al.*³⁹ On the dielectric surface from $x/L_e = 0.2$ to 4, the heat flux curve decreases smoothly. Dielectric heating occurs in the dielectric layer, in addition to the convective heat transfer of the heating gas. The total heat transfer on the surface typically increases within 1 s, reaching a constant value.

At a relatively high air pressure (filamentary mode), the trends of heat flux density with air pressure are different for the two applied voltages. At 25 kV and 1 kHz [Fig. 11(a)], the heat flux remains at a similar level (approximately 1500 W/m² at the peak value) for air pressures ranging from 1 to 0.4 bar. Comparatively, at 35 kV and 1 kHz [Fig. 11(d)], the maximum heat flux decreases markedly from 2400 to 500 W/m² when the air pressure drops from 1 to 0.2 bar. At 25 kV, 0.6 bar, and 1 kHz, the residual heat power is 0.12 W [Fig. 12(a)], even larger than the same air pressure case of 35 kV at 0.085 W [Fig. 12(d)]. This phenomenon, which agrees with the observation of discharge characteristics shown in Fig. 4, is stronger at high PRF, which indicates that the discharge intensity of a relatively high voltage heavily depends on the air density. Comparing Figs. 11(c) and 11(f) suggests that increasing the applied voltage may not increase the heat flux at moderate air pressures ranging from 0.6 to 0.8 bar. When PRF rises, the residual heat increases monotonically in both cases. Also, at 25 kV and 1 kHz, a low air pressure case at 0.4 bar retains a high residual heat value, while at 2 and 3 kHz, the residual heats decrease, indicating that there is a critical air density for different PRFs corresponding to the transition from the filamentary mode to the diffuse mode.

With the low air pressure at 0.4 bar in a diffuse discharge, the residual heat power suddenly drops to a lower level at 25 kV and PRF of 2 or 3 kHz but maintains this level when the air pressure further drops to 0.1 bar in both voltage cases. The maximum heat flux in the plasma region marginally decreases with pressure from 0.4 to 0.1 bar, but the heat flux in the original insulated region increases due to a longer plasma, leading to an irregular variation in the total heat [Figs. 12(a)–12(c)]. The residual heat power still increases monotonically with PRF. The heat increment caused by increasing voltage marginally reduces for the diffuse mode compared to the filamentary mode. A large residual heat

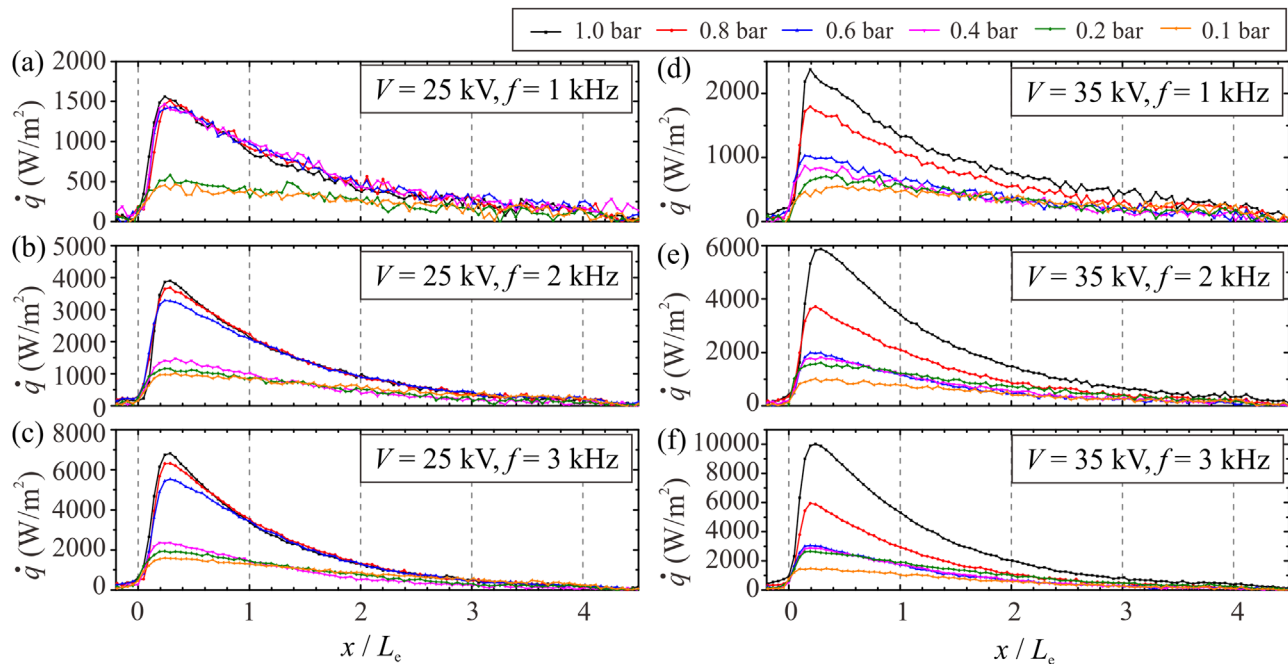


FIG. 11. Spanwise-averaged heat fluxes after the 10 000th pulse at 25 kV in the cases of (a) 1, (b) 2, and (c) 3 kHz and at 35 kV of (d) 1, (e) 2, and (f) 3 kHz.

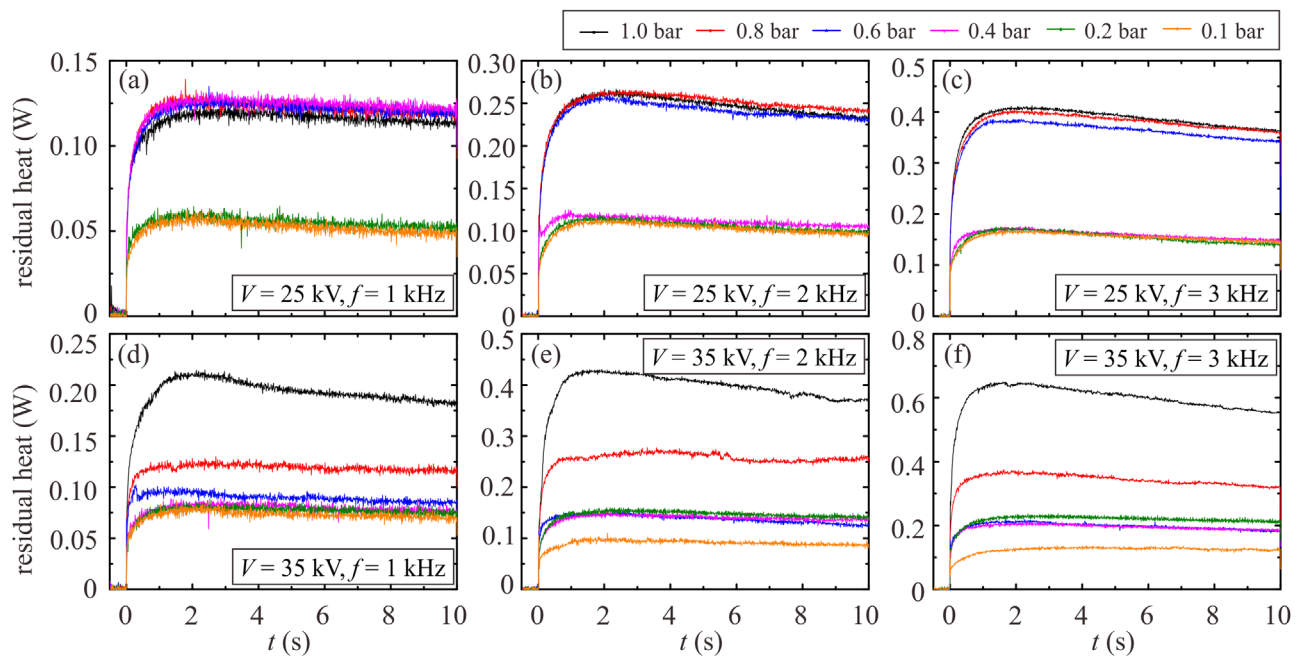


FIG. 12. Residual heat on the dielectric surface above the insulated electrode area in the rapid temperature increase stage in the cases of (a) 1, (b) 2, (c) 3 kHz at 25 kV, and (d) 1, (e) 2, (f) 3 kHz at 35 kV.

drop occurs at 0.1 bar at 35 kV and PRFs of 2 and 3 kHz, which may be caused by insufficient air for discharge under a high voltage and frequency power supply. These results imply that the applied voltage amplitude and PRF are not decisive factors in heat generation in diffuse mode and are even counterproductive under high voltage and high-frequency activation. Thus, heat transfer is strongly associated with the discharge mode. Compared to the diffuse mode, the gas heating process is more acute in the filamentary mode. At 25 kV, when the air pressure drops below a critical value, the heat transfer will jump from a high value to a low value. However, at a higher voltage of 35 kV, the surface heat transfer decreases with the air pressure drop accompanied by the attenuation of filaments and then remains at a constant value approximately in the diffuse mode (0.6 to 0.2 bar).

D. Induced shock wave dynamics and evolution of heated fluid

1. Induced shock structures and overpressure

The Schlieren images acquired at four typical times are shown in Fig. 13(a), where the frames show the shockwaves from the first, 100th, 1000th, and 10 000th pulses of 35 kV at 1 kHz. The induced shock wavefront consists of a semicylindrical shock and a planar shock. The semicylindrical shock expands from the alignment line of the exposed and insulated electrodes. Planar shock propagates upward parallel to the discharge streamers, which corresponds to the most gas heating in the discharge region. The shock structures are the same as those observed by Zhao *et al.*²⁹ and are produced through a quick pressure increase caused by the intense energy density in the discharge. Due to the residual heat near the surface, the shock wave propagation velocity reduces in subsequent pulses after a long time (e.g., the 10 000th pulse,

or after 10 s). This reduction in shock wave velocity is also substantiated in the overpressure measurements, presenting a longer time for the peak pressure to arrive at the sensor.

The overpressure of the induced shock can be captured as an abrupt pressure rise by the dynamic pressure sensor that remains at zero until the shock wave arrives at the monitoring points [Fig. 13(c)]. After the overpressure peak, there is a quick pressure drop, which is attributed to the rarefaction wave following the shock. This rarefaction wave is then reflected from the surface and catches up to the induced shock wavefront. Finally, the induced shock wave is weakened and decelerates to a sonic wave due to the interaction with the rarefaction waves.⁵⁴ The second peak at approximately 210 μ s that is shown in Fig. 13(c) is the reflection of the first shock wave between the copper shield over the sensor and the dielectric surface. To estimate the shock wave propagation velocity, the curve fitting was used by a displacement–time diagram. Figure 13(b) shows the wave propagation velocity through the Schlieren images, and the points indicate the shock front vertical positions above the anode–cathode edge, which are same as the measurement points of the pressure sensor. The darkest point with a local maximum intensity along the semicylindrical shock is identified as the shock front. The induced shock wave propagates at approximately 390 m/s ($Ma = 1.13$) at the beginning and rapidly attenuates to a sonic wave at 345 m/s under the interaction of the reflected rarefaction wave. The lower applied voltage amplitude of 25 kV leads to a lower initial velocity of 374 m/s ($Ma = 1.08$), which agrees with the observation of peak overpressure measurements. Due to the intense electromagnetic interference (EMI), the overpressure in the vicinity of the plasma region has rarely been reported in detail. The pressure profile can provide more information on the shock wave strength and further imply the interaction of shock and the surrounding gas.

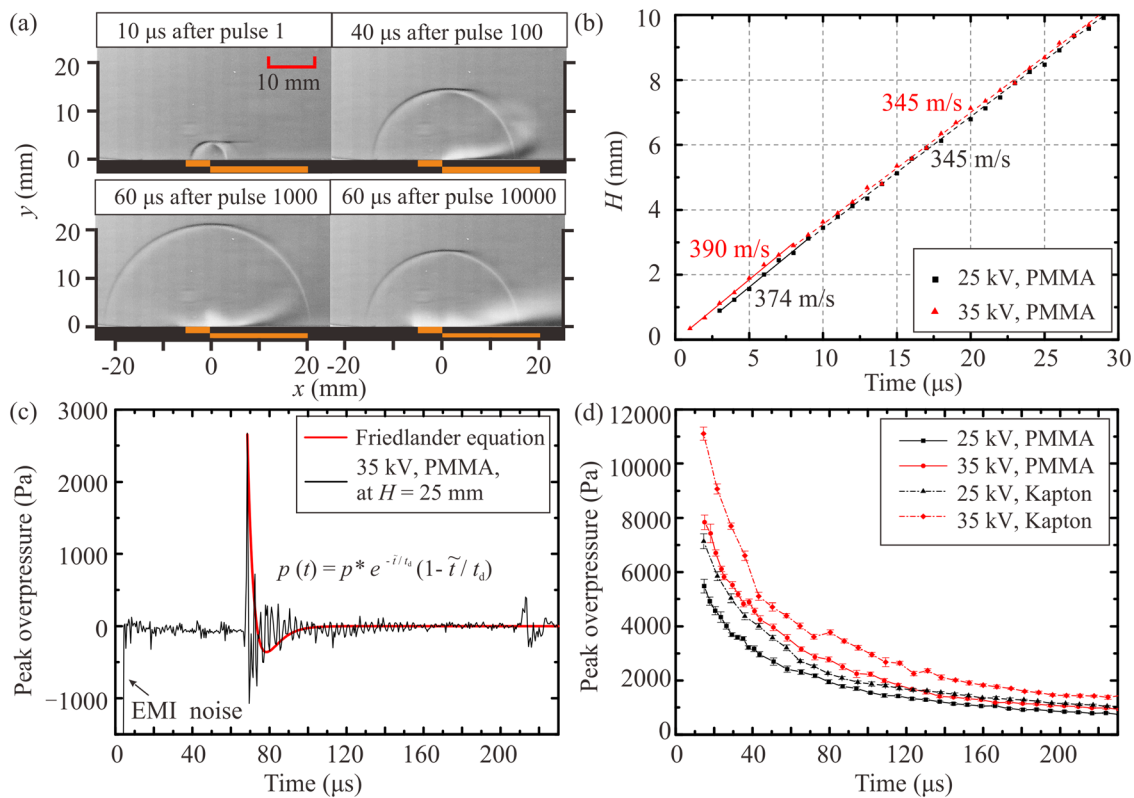


FIG. 13. (a) Schlieren images showing the induced shock structures and the residual heat in a repetitive case of 35 kV, 1 kHz; (b) the displacement vs time diagram of the peak overpressure with a curve fitting of shock velocity in Schlieren images; (c) the overpressure at $H = 25$ mm, $V = 35$ kV with curve fitting of Friedlander equation; (d) the peak overpressure as a function of the propagation time under a standard atmosphere.

Due to the protection provided by the copper shield, the minimum distance of the pressure sensor from the NSDBD actuator can be set to 5 mm in this study. However, a large negative signal remains in the measurement at the beginning of the activation and is likely caused by EMI noise that lasts approximately 5 μ s. Figure 13(d) shows the peak pressure of the induced shock wave created by the NSDBD plasma actuator vs the propagation time at a standard atmosphere, implying that the overpressure drops in an exponential fashion approximately as the shock propagates. Here, the values are the average peak overpressure for all pulses over the first 4 s. The pressure measurement for each case was repeated five times to fit the experimental repeatability. The peak pressure values are averaged over 1000 pulses at 1 kHz, and the standard errors are marked in the figure. The maximum value of the pressure peak is approximately 11 000 Pa at 35 kV with Kapton as the dielectric material and drops to 7000 Pa at a lower voltage amplitude. Another dielectric material of PMMA with the same thickness was used, and results showed that the different dielectric properties strongly affect the overpressure but with the same trend. Zhao *et al.*²⁹ believed that the shock wave generated by the NSDBD plasma actuator is fundamentally a blast wave, the strength and attenuation of which are strongly dependent on the voltage amplitude of the applied pulse. The time evolution of the shock pressure profile follows the Friedlander equation fairly well, as shown by the red curve in Fig. 13(c). This good fit indicates that the NSDBD plasma discharge actually exhibits a microblast wave.

Figure 14 shows the attenuation of the peak overpressure with time at different air pressures. The properties of varying air pressure shown in overpressures are consistent with the thermal performance associated with the discharge mode. First, in filamentary mode, the strength of the induced shock wave scarcely changes with air pressure under a lower voltage amplitude of 25 kV [see black, red, and blue lines in Figs. 14(a)–14(c)] but deviates markedly at 35 kV. Second, in the transition mode, the peak overpressure quickly decreases, accompanied by a larger fluctuation that indicates an unsteady discharge state. Third, in the diffuse mode at 0.1 bar pressure, the strength of the induced shock wave drops below 1000 Pa, which is only one-eighth of that at standard pressure, at both voltages. This similarity to thermal features also indicates that the induced shock wave is generated by the fast-heating process; the PRF does little work on the strength of overpressure.

2. Development of the heated fluid

The starting vortex is also an important characteristic of the induced flow caused by the plasma actuator. The development of the starting vortex is described in Fig. 15. The multiple repeated measurements indicate that the development process is similar in the same case. Therefore, only one evolution sequence of each case shown hereinafter. When the plasma is generated, the residual heat is deposited rapidly in the discharge region. As shown in Fig. 15(b1)

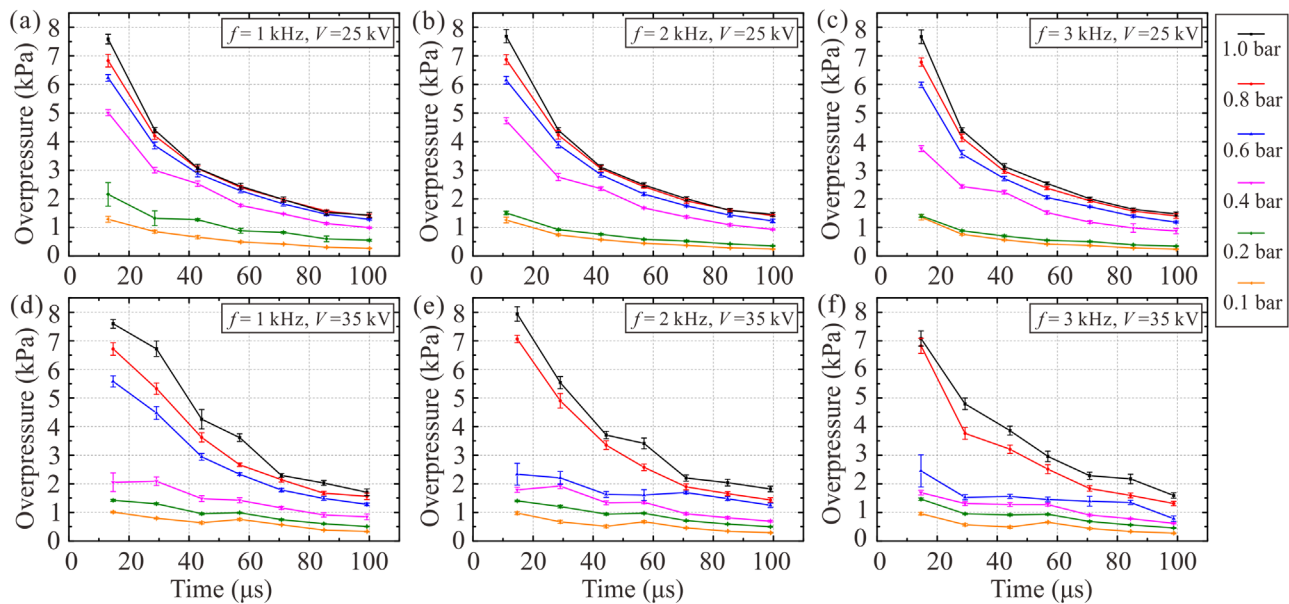


FIG. 14. Time-averaged peak overpressure under different air pressures of the 25 kV cases at (a) 1, (b) 2, and (c) 3 kHz and the 35 kV cases at (d) 1, (e) 2, and (f) 3 kHz.

(Multimedia view), the heat transfers to the surrounding air and forms a hotspot area that is completely decoupled from the induced compression waves. Each single pulse intensifies the heating in this region and expands thermally to the vicinity.⁵⁵ The hotspot area is concentrated upstream of the discharge streamer, which is consistent with the regions of the maximum luminosity and fastest temperature increase. The ionized particles move toward the dielectric surface under the body force produced by the strong electric field. Due to the short effect time of the electric field (nanosecond scale for each pulse), the movement of thermal fluid is more sluggish than the deposition of heat. To replenish the fluid that was ejected downstream, the fluid upstream of the plasma region is entrained and rolls up to form a starting vortex in the jet front, as shown in Fig. 15(a2). The vorticity originates at the transient front, which is similar to a wedge of vorticity intruding into an inviscid region.⁵⁶ The vorticity fronts form in a shear flow as the result of fast patches of fluid catching up with slower ones.

The front of the nose steepens and propagates later, “backward” wave breaking occurs, and outer irrotational fluid is entrained.⁵⁶ Due to the velocity gradient near the wall, negative vorticity was observed at the wall. Conlon and Lichter⁵⁷ believed that the wall will cause a bias to the initial shear layer where the circulation associated with the positive vorticity will be greater than that associated with the negative vorticity. The initially quiescent domain exerts its influence on the relative amounts of positive and negative vorticities through the proximity of the jet to the boundary. Due to the growth of the secondary vorticity and the interaction between positive and negative vorticities, the positive vortex will be pushed into the outer irrotational ambient flow.⁵⁸ The vortex generation in the vorticity front and separation of the jet from the wall arise, not from vorticity diffusing in from the boundary or from a Kelvin–Helmholtz instability, occurs for a steady wall jet.⁵⁷ Because the high-temperature fluid will move downstream to form a vortex and cause a change in the density gradient, the formation of the

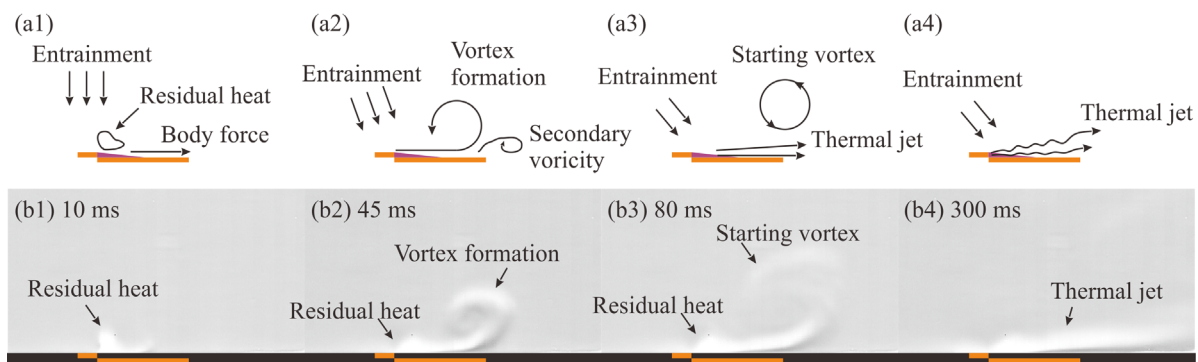


FIG. 15. (a) Schematic of the development of the starting vortex and thermal jet and (b) Schlieren images in the case of 35 kV and 3 kHz at standard atmosphere. Multimedia view: <https://doi.org/10.1063/5.0127251.2>

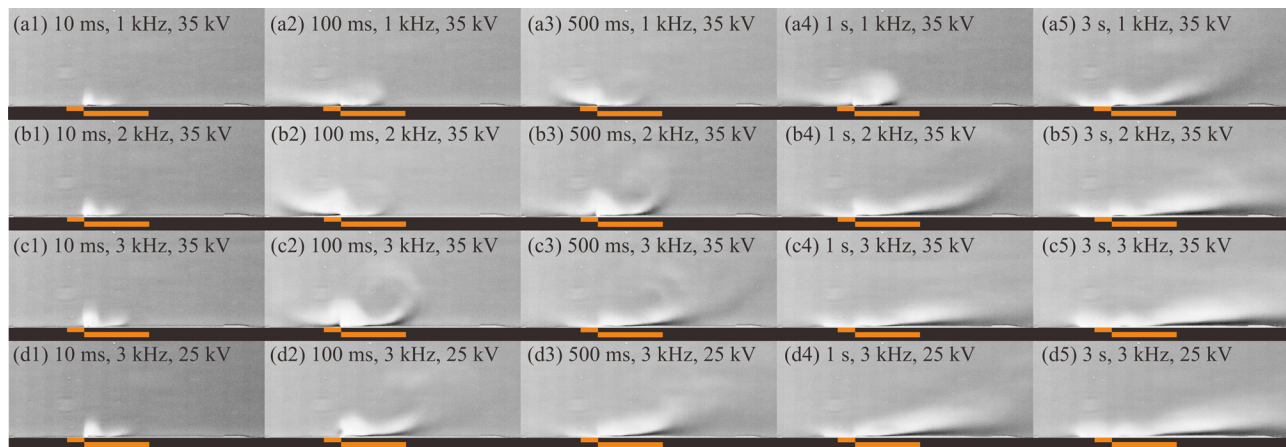


FIG. 16. Evolution of residual heat of the NSDBD of 35 kV at (a1)–(a5) 1 kHz, (b1)–(b5) 2 kHz, (c1)–(c5) 3 kHz, and (d1)–(d5) 3 kHz of 25 kV at a standard atmosphere.

starting vortex can be captured by the Schlieren images in Figs. 15(b2) and 15(b3). Estimated from the Schlieren images, the vortex structure propagates with a velocity of approximately 0.3 m/s and remains for a period longer than 80 ms. To preserve the no-slip boundary condition, secondary vorticity is generated at the wall and wraps around the starting vortex to steer the trajectory away from the wall,⁵⁹ as shown in Fig. 15(b3). The starting vortex becomes weaker and repeatedly breaks down under the impact of the induced shock waves. Finally, a steady wall jet with a high temperature is formed, similar to an ACDBD plasma actuator.⁶⁰ Zhao *et al.*²⁹ measured the transient flow behind the moving shock wave at a speed of up to 35 m/s. The induced jet becomes turbulent, which can be attributed to the combined effects of the impact of induced flow moving with the shock wave, the localized convection caused by the heated actuator surface, and the pulsed energy thermalization in the discharge filaments.⁶¹ The maximum velocity of the induced jet is typically no more than 1 m/s, which is

markedly smaller than that generated by the ACDBD plasma actuator of 8 m/s. The additional momentum caused by the induced jet no longer plays the dominant role in the flow control using the NSDBD plasma actuator.

The evolution of residual heat with different PRFs is plotted in Fig. 16 at a standard atmosphere. Increasing PRF results in a quicker fluid movement downstream, a larger residual heat region, and heat convection reduction to the upstream fluid. A more extended thermal jet, which is markedly longer than the insulated electrode length, can be observed with a high PRF [Figs. 16(a5), 16(b5), and 16(c5)]. A large portion of the heat is convected downstream under the ionized wind. The lower applied voltage case with the same PRF shares a similar evolution but has an marked contractible residual heat region. The case of 25 kV at 3 kHz is considered to demonstrate the evolution of residual heat at the different air pressures, as shown in Fig. 17. When the discharge is shifted to the diffuse mode at 0.4 bar, the residual heat prefers

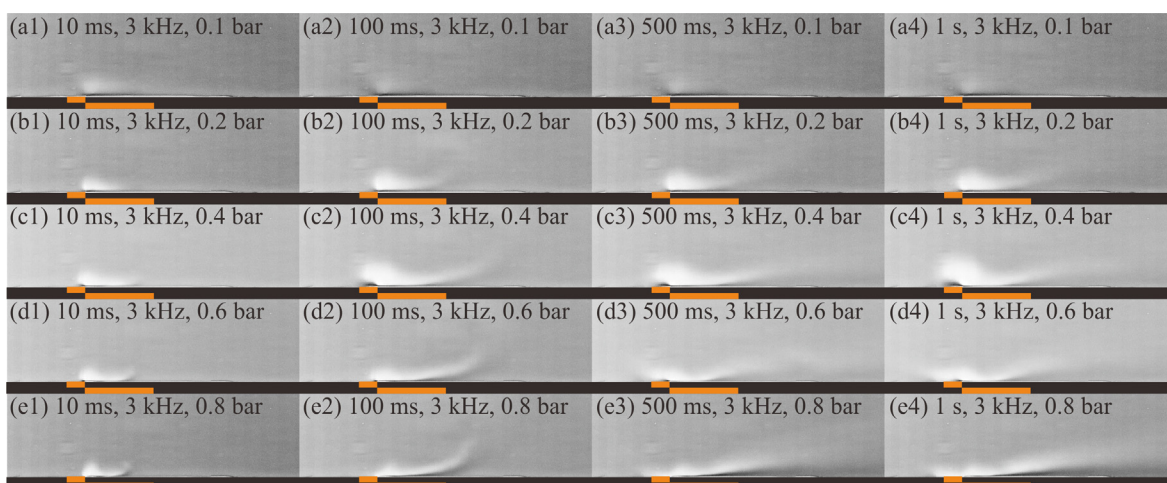


FIG. 17. Evolution of residual heat generated by the NSDBD plasma actuator, which is operated at 3 kHz of 25 kV under ambient pressures of (a1)–(a4) 0.1 bar, (b1)–(b4) 0.2 bar, (c1)–(c4) 0.4 bar, (d1)–(d4) 0.6 bar, and (e1)–(e4) 0.8 bar.

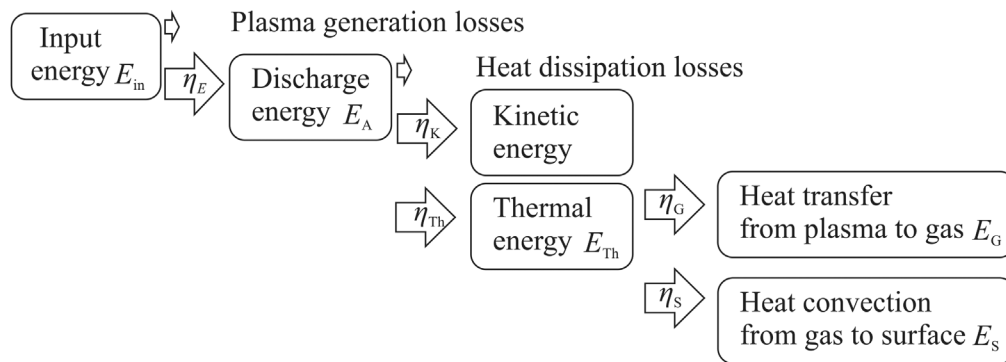


FIG. 18. Schematic of the energy budget of an NSDBD plasma actuator.

to convect vertically from the surface (larger residual heat region) due to a thicker plasma region, which also explains the reduction in heat convection on the dielectric surface. The thermal jet lifts off from the wall surface because the fluid in the discharge region has a lower density through the fast-heating process and then accelerates under the electric field. Therefore, the heat convection in the far-field region on the wall surface plays a relatively minor role in the surface temperature increase. However, because the Schlieren images measure the density gradient normal to the knife direction, the low air density will directly affect the measurement sensitivity. Therefore, the changes under 0.1 bar are debatable. However, the discharge is strongly weakened at a lower air density.

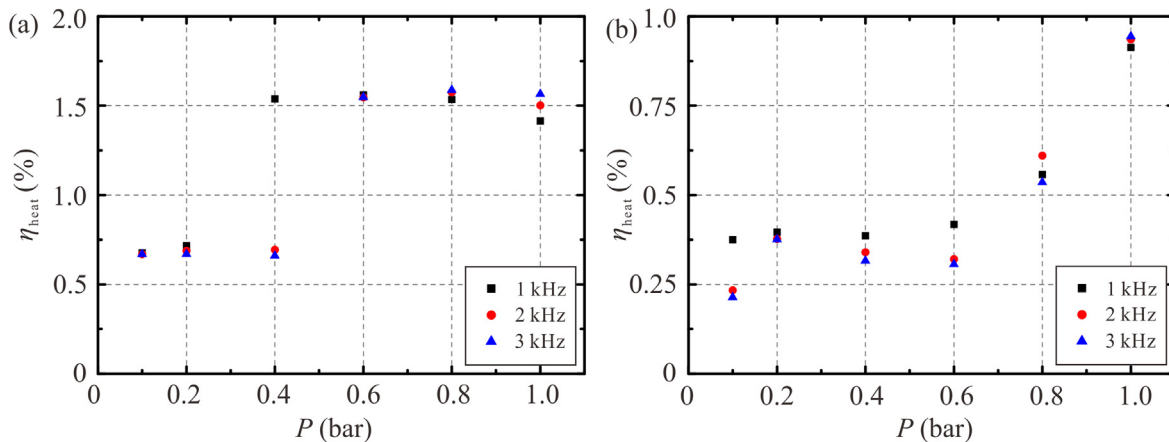
E. Heat efficiency

The definition of the energy stages was clarified by Kriegseis *et al.*⁶² and improved by Liu *et al.*,³⁶ as shown in Fig. 18. The efficiency of the first operational stage is defined as the ratio between the discharge energy E_A and the electrical input energy E_{in} .³⁹ The efficiency of the second stage is defined as the ratio between the output energy (kinetic and thermal energy) and discharge energy. Because the control mechanism of an NSDBD plasma actuator is based on a thermal effect, this study aims to estimate the thermal energy efficiency,

which is necessary for engineering such as anti-icing. The heating efficiency is defined as the ratio of thermal energy on the dielectric surface E_{heat} and total energy input E_{in} , as shown in Eq. (2). In this study, E_{heat} includes the heat convection from the gas to the surface (E_s) and heat generation by the dielectric losses:

$$\eta_{heat} = \frac{E_{heat}}{E_{in}}. \quad (7)$$

The surface heating efficiency η_{heat} was calculated by Eq. (7) using the integration of heat flux on the dielectric surface. The η_{heat} shown in Fig. 19 is the average value of repeated measurements. η_{heat} is small, ranging from 0.5% to 2% with an uncertainty of 0.046% ($\sim 2.8\%$ of the mean value), similar to the observation of Liu *et al.*³⁶ As shown in Fig. 19, the reduction in air pressure would heavily affect the heating efficiency, with the heating process being more efficient at high air pressure. Under a relatively low voltage, the figure shows two states that are relevant to the discharge mode. The air pressure change in the respective discharge mode would not influence the heating efficiency. However, at high voltage, the heating efficiency decreases with thinner air in filamentary mode due to the weaker discharge filaments. PRF rarely affects the heating efficiency, although the absolute heat strongly increases with a high PRF. In the diffuse mode at 35 kV, a high PRF

FIG. 19. Surface heating efficiency η_{heat} under different air pressures at (a) 25 kV and (b) 35 kV.

marginally decreases the heating efficiency. Aleksandrov *et al.*⁶³ reported that most of the thermal energy generated in the plasma is stored in the gas layer near the surface. The thermal energy efficiency η_{Th} from the discharge is relatively higher and varies from 40% to 90%.^{16,39,64} In this study, the large fluctuation range of η_{Th} is caused by the uncertainties in measuring the thermal energy of hot gas by different authors. Due to the low heating efficiency on the surface, it remains a challenge in real applications of NSDBD plasma actuators, such as icing mitigation on aircraft.

IV. CONCLUSION

In this paper, the characteristics of an NSDBD at different air pressures are investigated in detail to explore the engineering potential for flow control. Comparisons in the cases of air pressure ranging from 0.1 to 1 bar at 25 and 35 kV with PRFs of 1, 2, 3 kHz are made. Detailed results are summarized as follows:

- (1) By measuring the applied voltage and current, results show that energy input increases with the applied voltage and only slightly depends on the gas pressure. By observing discharge features, the transition from a filamentary mode to a diffuse mode with decreasing air pressure is described. The filamentary streamers extend along the radius direction, forming a more stable, uniform, thicker plasma region because the ionized volume should be increased due to the sparse air to maintain the high values of the reduced electric field. Although the PRF plays an important role in the flow control, it only slightly affects the streamer distribution, luminosity, and discharge mode transition with changes in air pressure.
- (2) The spatiotemporal temperature distribution on the surface indicates that the heated surface can be divided into three typical regions in the streamwise direction: the plasma region, the insulated electrode region, and the far-field region distinguished by two inflection points. Because gas heating is generated during quenching of the excited molecules, the maximum temperature increase on the surface occurs in the plasma region and attenuates downstream. The surface temperature increase is primarily caused by heat convection from the residual heat in plasma and the heat generated by the dielectric losses.
- (3) The thermal effects are strongly associated with the discharge mode. Compared to the diffuse mode, the gas heating process is more acute in a filamentary mode. At 25 kV, when the air pressure drops below a critical value, the heat transfer will jump from a high to low value. However, at a higher voltage of 35 kV, the surface heat transfer decreases with the air pressure drop accompanied by the attenuation of filaments and then remains at a value in the diffuse mode. Choosing the most appropriate applied voltage and PRF based on discharge characteristics will strongly increase the control efficiency. In the future, better performance cases will be used for continuing study, especially how to increase gas heating efficiency further.
- (4) The hydrodynamics of the induced shock wave and its strength are also investigated. Results show that the overpressure drops approximately exponentially with the shock spread. The induced shock wave propagates at approximately 390 m/s ($Ma = 1.13$) at the beginning and rapidly attenuates to a sonic wave at 345 m/s under the interaction of the reflected rarefaction wave. The time evolution of the shock pressure profile generally

follows the Friedlander equation and indicates that the NSDBD plasma discharge actually achieves a microblast wave characteristic. The similarity between the overpressure strength and thermal features also shows that the induced shock wave is generated from the fast heating process. The evolution of a starting vortex and a steady wall jet is similar to that of an ACDBD plasma actuator. In diffuse mode at 0.4 bar, the residual heat prefers to convect vertically from the surface with a larger residual heat region due to a thicker plasma region. Eventually, the thermal jet lifts off from the wall surface because the expanded thermal fluid accelerates under the electric field.

- (5) The results indicate that the heating efficiency on the surface ranges from 0.5% to 2%. The low heating efficiency on the surface suggests that there is still a challenge for the application of NSDBD plasma actuators.

The results in this study can also help establish a more exact thermodynamic model of NSDBD plasma actuation, particularly in the extreme cases of high voltage and PRFs. The results of this study also provide references for the mechanism detection of icing mitigation and flow control based on NSDBD plasma actuators. In future work, the variation characteristics of the spatial temperature field should be investigated in more detail to quantitatively evaluate the heat in the gas.

ACKNOWLEDGMENTS

The authors are grateful for the financial support provided by the Hong Kong Research Grants Council (No. PolyU15217622).

AUTHOR DECLARATIONS

Conflict of Interest

The authors have no conflicts to disclose.

Author Contributions

Zongnan Chen: Investigation (lead); Writing – original draft (equal). **Chung Chu Wong:** Investigation (equal). **Chih-Yung Wen:** Conceptualization (equal); Funding acquisition (equal); Supervision (equal).

DATA AVAILABILITY

The data that support the findings of this study are available from the corresponding author upon reasonable request.

REFERENCES

- ¹M. Gad-el-Hak, *Flow Control: Passive, Active, and Reactive Flow Management* (Cambridge University Press, 2000), p. 421.
- ²J. G. Zheng, Y. D. Cui, Z. J. Zhao, J. Li, and B. C. Khoo, "Investigation of airfoil leading edge separation control with nanosecond plasma actuator," *Phys. Rev. Fluids* **1**(7), 073501 (2016).
- ³J. Little, K. Takashima, M. Nishihara, I. Adamovich, and M. Samimy, "Separation control with nanosecond-pulse-driven dielectric barrier discharge plasma actuators," *AIAA J.* **50**(2), 350–365 (2012).
- ⁴R. Sosa, J. D'Adamo, and G. Artana, "Circular cylinder drag reduction by three-electrode plasma actuators," *J. Phys.* **166**, 012015 (2009).
- ⁵F. O. Thomas, T. C. Corke, A. Duong, S. Midya, and K. Yates, "Turbulent drag reduction using pulsed-DC plasma actuation," *J. Phys. D* **52**(43), 434001 (2019).

- ⁶X. Huang and X. Zhang, "Streamwise and spanwise plasma actuators for flow-induced cavity noise control," *Phys. Fluids* **20**(3), 037101 (2008).
- ⁷F. O. Thomas, A. Kozlov, and T. C. Corke, "Plasma actuators for cylinder flow control and noise reduction," *AIAA J.* **46**(8), 1921–1931 (2008).
- ⁸Z. Chen, L. Shen, and C.-Y. Wen, "Flow control on a bluff body using dielectric barrier discharge plasma actuators," *AIAA J.* **57**(7), 2670–2674 (2019).
- ⁹Z. Chen and C.-Y. Wen, "Flow control of a D-shaped bluff body using different DBD plasma actuators," *J. Fluids Struct.* **103**, 103292 (2021).
- ¹⁰M. Belan and F. Messanelli, "Compared ionic wind measurements on multi-tip corona and DBD plasma actuators," *J. Electrostat.* **76**, 278–287 (2015).
- ¹¹M. Tang, Y. Wu, H. Wang, S. Guo, Z. Sun, and J. Sheng, "Characterization of transverse plasma jet and its effects on ramp induced separation," *Exp. Therm. Fluid Sci.* **99**, 584–594 (2018).
- ¹²F. Liu, H. Yan, W. Zhan, and Y. Xue, "Effects of steady and pulsed discharge arcs on shock wave control in Mach 2.5 flow," *Aerosp. Sci. Technol.* **93**, 105330 (2019).
- ¹³L. Shen, C.-Y. Wen, and H.-A. Chen, "Asymmetric flow control on a delta wing with dielectric barrier discharge actuators," *AIAA J.* **54**(2), 652–658 (2016).
- ¹⁴L. Shen, Z. N. Chen, and C.-Y. Wen, "Experimental investigation of the flow structure over a delta wing via flow visualization methods," *J. Vis. Exp.* **134**, 57244 (2018).
- ¹⁵M. Nudnova, S. Kindusheva, and N. Aleksandrov, "Rate of plasma thermalization of pulsed nanosecond surface dielectric barrier discharge," paper presented at the 8th AIAA Aerospace Sciences Meeting Including the New Horizons Forum and Aerospace Exposition, Orlando, Florida, 2010.
- ¹⁶G. Correale, R. Winkel, and M. Kotsonis, "Energy deposition characteristics of nanosecond dielectric barrier discharge plasma actuators: Influence of dielectric material," *J. Appl. Phys.* **118**(8), 083301 (2015).
- ¹⁷L. Shen, Z. N. Chen, and C.-Y. Wen, "Thermal effect on the performance of an alternating-current dielectric-barrier-discharge plasma actuator," *AIAA J.* **58**(8), 3368–3377 (2020).
- ¹⁸X. Zhang, Y. D. Cui, C.-M. J. Tay, and B. C. Khoo, "Ultrasound generated by alternating current dielectric barrier discharge plasma in quiescent air," *Plasma Sources Sci. Technol.* **29**(1), 015017 (2020).
- ¹⁹D. V. Roupasov, A. A. Nikipelov, M. M. Nudnova, and A. Y. Starikovskii, "Flow separation control by plasma actuator with nanosecond pulsed-periodic discharge," *AIAA J.* **47**(1), 168–185 (2009).
- ²⁰S. Chen, Z. Shi, Z. Zhao, X. Geng, and Z. Chen, "Investigation of vertical tail buffeting alleviation controlled by nanosecond plasma actuators," *Phys. Fluids* **33**(8), 087109 (2021).
- ²¹H. Yu and J. Zheng, "Numerical investigation of control of dynamic stall over a NACA0015 airfoil using dielectric barrier discharge plasma actuators," *Phys. Fluids* **32**(3), 035103 (2020).
- ²²Y. D. Cui, Z. J. Zhao, J. Li, J. G. Zheng, and B. C. Khoo, "Flow separation control over a ramp with nanosecond-pulsed plasma actuators," paper presented at the Proceedings of 30th International Symposium on Shock Waves 2, 2017.
- ²³Z.-J. Zhao, Y. D. Cui, J.-M. Li, J.-G. Zheng, and B. C. Khoo, "On the boundary flow using pulsed nanosecond DBD plasma actuators," *Mod. Phys. Lett. B* **32**(12n13), 1840035 (2018).
- ²⁴M. Nishihara, K. Takashima, J. W. Rich, and I. V. Adamovich, "Mach 5 bow shock control by a nanosecond pulse surface dielectric barrier discharge," *Phys. Fluids* **23**(6), 066101 (2011).
- ²⁵N. J. Bisek, J. Poggie, M. Nishihara, and I. Adamovich, "Hypersonic flow over a cylinder with a nanosecond pulse electrical discharge," *J. Thermophys. Heat Transfer* **28**(1), 18–26 (2014).
- ²⁶J. G. Zheng, Y. D. Cui, J. Li, and B. C. Khoo, "A note on supersonic flow control with nanosecond plasma actuator," *Phys. Fluids* **30**(4), 040907 (2018).
- ²⁷K. Kinefuchi, A. Y. Starikovskii, and R. B. Miles, "Control of shock-wave/boundary-layer interaction using nanosecond-pulsed plasma actuators," *J. Propul. Power* **34**(4), 909–919 (2018).
- ²⁸K. Kinefuchi, A. Y. Starikovskii, and R. B. Miles, "Numerical investigation of nanosecond pulsed plasma actuators for control of shock-wave/boundary-layer separation," *Phys. Fluids* **30**(10), 106105 (2018).
- ²⁹Z. Zhao, J.-M. Li, J. Zheng, Y. D. Cui, and B. C. Khoo, "Study of shock and induced flow dynamics by nanosecond dielectric-barrier-discharge plasma actuators," *AIAA J.* **53**(5), 1336–1348 (2015).
- ³⁰C. Zhang, B. Huang, Z. Luo, X. Che, P. Yan, and T. Shao, "Atmospheric-pressure pulsed plasma actuators for flow control: Shock wave and vortex characteristics," *Plasma Sources Sci. Technol.* **28**(6), 064001 (2019).
- ³¹A. C. A. Ndong, N. Zouzou, N. Benard, and E. Moreau, "Geometrical optimization of a surface DBD powered by a nanosecond pulsed high voltage," *J. Electrostat.* **71**(3), 246–253 (2013).
- ³²C. Kolbakir, Y. Liu, H. Hu, A. Starikovskii, and R. B. Miles, "An experimental investigation on the thermal effects of NS-DBD and AC-DBD plasma actuators for aircraft icing mitigation," AIAA Paper No. 2018-0164 (2018).
- ³³Y. Liu, C. Kolbakir, H. Hu, X. Meng, and H. Hu, "An experimental study on the thermal effects of duty-cycled plasma actuation pertinent to aircraft icing mitigation," *Int. J. Heat Mass Transfer* **136**, 864–876 (2019).
- ³⁴B. Wei, Y. Wu, H. Liang, J. Chen, G. Zhao, M. Tian, and H. Xu, "Performance and mechanism analysis of nanosecond pulsed surface dielectric barrier discharge based plasma deicer," *Phys. Fluids* **31**(9), 091701 (2019).
- ³⁵L. Xie, H. Liang, H. Zong, X. Liu, and Y. Li, "Multipurpose distributed dielectric-barrier-discharge plasma actuation: Icing sensing, anti-icing, and flow control in one," *Phys. Fluids* **34**(7), 071701 (2022).
- ³⁶Y. Liu, C. Kolbakir, A. Y. Starikovskii, R. Miles, and H. Hu, "An experimental study on the thermal characteristics of NS-DBD plasma actuation and application for aircraft icing mitigation," *Plasma Sources Sci. Technol.* **28**(1), 014001 (2019).
- ³⁷A. Y. Starikovskii, A. A. Nikipelov, M. M. Nudnova, and D. V. Roupasov, "SDBD Plasma actuator with nanosecond pulse-periodic discharge," *Plasma Sources Sci. Technol.* **18**(3), 034015 (2009).
- ³⁸K. Takashima, Y. Zuzeev, W. R. Lempert, and I. V. Adamovich, "Characterization of a surface dielectric barrier discharge plasma sustained by repetitive nanosecond pulses," *Plasma Sources Sci. Technol.* **20**(5), 055009 (2011).
- ³⁹G. Correale, F. Avallone, and A. Y. Starikovskii, "Experimental method to quantify the efficiency of the first two operational stages of nanosecond dielectric barrier discharge plasma actuators," *J. Phys. D* **49**(50), 505201 (2016).
- ⁴⁰M. M. Nudnova, S. V. Kindusheva, N. L. Aleksandrov, and A. Y. Starikovskii, "Fast gas heating in N₂/O₂ mixtures under nanosecond surface dielectric barrier discharge: The effects of gas pressure and composition," *Philos. Trans. R. Soc. A* **373**(2048), 20140330 (2015).
- ⁴¹C. Ding, A. Y. Khomenko, S. A. Shcherbanev, and S. M. Starikovskaia, "Filamentary nanosecond surface dielectric barrier discharge. Experimental comparison of the streamer-to-filament transition for positive and negative polarities," *Plasma Sources Sci. Technol.* **28**(8), 085005 (2019).
- ⁴²W. J. Cook and E. J. Felderman, "Reduction of data from thin-film heat-transfer gages: A concise numerical technique," *AIAA J.* **4**(3), 561–562 (1966).
- ⁴³Y. Zhu, D. Gu, W. Zhu, S. Chen, C. Lee, and E. S. Oran, "Dilatational-wave-induced aerodynamic cooling in transitional hypersonic boundary layers," *J. Fluid Mech.* **911**, A36 (2021).
- ⁴⁴M. Zhang, W. Si, and C. Lee, "Heat transfer and recovery factor of aerodynamic heating on a flared cone," *AIAA J.* **59**(11), 4284–4292 (2021).
- ⁴⁵J. Lawrence, A. B. Patel, and J. G. Brissin, "The thermal conductivity of Kapton Hn between 0.5 and 5 K," *Cryogenics* **40**, 203–207 (2000).
- ⁴⁶V. I. Gibalov and G. J. Pietsch, "The development of dielectric barrier discharges in gas gaps and on surfaces," *J. Appl. Phys.* **33**(20), 2618–2636 (2000).
- ⁴⁷M. Simeni Simeni, Y. Tang, K. Frederickson, and I. V. Adamovich, "Electric field distribution in a surface plasma flow actuator powered by ns discharge pulse trains," *Plasma Sources Sci. Technol.* **27**(10), 104001 (2018).
- ⁴⁸C.-W. Yao, Z.-S. Chang, H. Ma, G. Xu, H. Mu, and G.-J. Zhang, "Experimental research on mode transitions of atmospheric pressure helium dielectric barrier discharge," *IEEE Trans. Plasma Sci.* **44**(11), 2576–2588 (2016).
- ⁴⁹N. A. Popov, "Investigation of the mechanism for rapid heating of nitrogen and air in gas discharges," *Plasma Phys. Rep.* **27**(10), 886–896 (2001).
- ⁵⁰J. C. Tully, "Reactions of O(¹D) with atmospheric molecules," *J. Chem. Phys.* **62**(5), 1893–1898 (1975).
- ⁵¹N. A. Popov, "Fast gas heating in a nitrogen-oxygen discharge plasma: I. Kinetic mechanism," *J. Phys. D* **44**(28), 285201 (2011).
- ⁵²S. Lanier, I. Shkurenkov, I. V. Adamovich, and W. R. Lempert, "Two-stage energy thermalization mechanism in nanosecond pulse discharges in air and hydrogen-air mixtures," *Plasma Sources Sci. Technol.* **24**(2), 025005 (2015).

- ⁵³N. Y. Babaeva, D. V. Tereshonok, and G. V. Naidis, "Fluid and hybrid modeling of nanosecond surface discharges: Effect of polarity and secondary electrons emission," *Plasma Sources Sci. Technol.* **25**(4), 044008 (2016).
- ⁵⁴Z. Chen, J. Hao, and C.-Y. Wen, "Control of supersonic compression corner flow using a plasma actuator," *Phys. Fluids* **34**(7), 073605 (2022).
- ⁵⁵T. Ukai, A. Russell, H. Zare-Behtash, and K. Kontis, "Temporal variation of the spatial density distribution above a nanosecond pulsed dielectric barrier discharge plasma actuator in quiescent air," *Phys. Fluids* **30**(11), 116106 (2018).
- ⁵⁶M. E. Stern and L. J. Pratt, "Dynamics of vorticity fronts," *J. Fluid Mech.* **161**(1), 513 (1985).
- ⁵⁷B. P. Conlon and S. Lichter, "Dipole formation in the transient planar wall jet," *Phys. Fluids* **7**(5), 999–1014 (1995).
- ⁵⁸F. B. Hsiao and S. S. Sheu, "Double row vortical structures in the near region of a plane wall jet," *Exp. Fluids* **17**, 291–301 (1994).
- ⁵⁹R. D. Whalley and K.-S. Choi, "The starting vortex in quiescent air induced by dielectric-barrier-discharge plasma," *J. Fluid Mech.* **703**, 192–203 (2012).
- ⁶⁰B. K. Mishra and P. K. Panigrahi, "Flow field induced by a dielectric barrier discharge plasma actuator analyzed with bi-orthogonal decomposition," *Phys. Fluids* **32**(8), 087112 (2020).
- ⁶¹A. Montello, D. Burnette, M. Nishihara, W. R. Lempert, and I. V. Adamovich, "Dynamics of rapid localized heating in nanosecond pulse discharges for high speed flow control," *J. Fluid Sci. Technol.* **8**(2), 147–159 (2013).
- ⁶²J. Kriegseis, A. Duchmann, C. Tropea, and S. Grundmann, "On the classification of dielectric barrier discharge plasma actuators: A comprehensive performance evaluation study," *J. Appl. Phys.* **114**(5), 053301 (2013).
- ⁶³N. L. Aleksandrov, S. V. Kindysheva, M. M. Nudnova, and A. Y. Starikovskiy, "Mechanism of ultra-fast heating in a non-equilibrium weakly ionized air discharge plasma in high electric fields," *J. Phys. D* **43**(25), 255201 (2010).
- ⁶⁴J. Van de Broecke, "De-icing using NS-DBD plasma actuators," Master thesis (Faculty of Aerospace Engineering, Delft University of Technology, 2016).